
# RIS-Enabled SISO Localization under User Mobility and Spatial-Wideband Effects



Citation for the original published paper (version of record):
Keykhosravi, K., Keskin, F., Seco-Granados, G. et al (2022). RIS-Enabled SISO Localization under User Mobility and Spatial-Wideband Effects. IEEE Journal on Selected Topics in Signal Processing, 16(5): 1125-1140. http://dx.doi.org/10.1109/JSTSP.2022.3175036



(article starts on next page)

# RIS-Enabled SISO Localization under User Mobility and Spatial-Wideband Effects

Kamran Keykhosravi, *Member, IEEE,* Musa Furkan Keskin, *Member, IEEE,* Gonzalo Seco-Granados, *Senior Member, IEEE,* Petar Popovski, *Fellow, IEEE,* and Henk Wymeersch, *Senior Member, IEEE.*

***Abstract*—Reconfigurable intelligent surface (RIS) is a promising technological enabler for the 6th generation (6G) of wireless systems with applications in localization and communication. In this paper, we consider the problem of positioning a single-antenna user in 3D space based on the received signal from a single-antenna base station and reflected signal from an RIS by taking into account the mobility of the user and spatial-wideband (WB) effects. To do so, we first derive the spatial-WB channel model under the far-field assumption, for orthogonal frequency-division multiplexing signal transmission with the user having a constant velocity. We derive the Cramér Rao bounds to serve as a benchmark. Furthermore, we devise a low-complexity estimator that attains the bounds in high signal-to-noise ratios. Our estimator neglects the spatial-WB effects and deals with the user mobility by estimating the radial velocities and compensating for their effects in an iterative fashion. We show that the spatial-WB effects can degrade the localization accuracy for large RIS sizes and large signal bandwidths as the direction of arrival or departure deviate from the RIS normal. In particular, for a 64 $\times$ 64 RIS, the proposed estimator is resilient against the spatial-WB effects up to 140 MHz bandwidth. Regarding user mobility, our results suggest that the velocity of the user influences neither the bounds nor the accuracy of our estimator. Specifically, we observe that the state of the user with a high speed (42 m/s) can be estimated virtually with the same accuracy as a static user.**

***Index Terms*—Reconfigurable intelligent surface, position error bound, Cramér-Rao bound, radio localization, spatial-wideband.**

## I. Introduction

Estimation of user location has become increasingly crucial in today's networking technology with applications in autonomous driving, navigation, data transmission, augmented reality, etc. [2]. Satellite localization systems such as the global positioning system (GPS) have the downside that they do not function properly in indoor scenarios, urban canyons, or tunnels. As a complementary approach, cellular localization can be used, where the user state is estimated based on the radio signals interchanged between the base station (BS) and the user. Provisioning of cellular localization was stirred by the governmental authorities demanding that the operators should provide the location of the user equipment (UE) upon receiving emergency calls. In 4G wireless systems, the UE location and clock bias are estimated by calculating time-difference-of-arrival (TDoA) between the UE and four synchronized BSs [3]. In 5G, the multi-antenna structure of BSs and UEs allowed networks to also use the angles of arrival and departure for localization, enabling positioning with one BS under rich multipath conditions [4]. In this work, we show that the next generation, 6G, can benefit from the new technological enablers, such as reconfigurable intelligent surfaces (RISs), to estimate the UE position, clock bias, and velocity, even for single-input single-output (SISO) wireless links.

RISs are thin surfaces made of sub-wavelength unit cells, whose response to the impinging electromagnetic wave can be controlled [5]. Recently, a great deal of attention has been drawn to RISs as one of the foremost technological enablers of the next generation of wireless systems (see [6] for an excellent literature review). RISs introduce a new paradigm in wireless systems since they enable the optimization of the channel to maximize the quality of service (QoS) [7]–[10]. In a communication system, where the RIS response can be optimized to improve the signal-to-noise ratio (SNR) and the spectral efficiency at the UE site, the main challenges pertain to path loss modeling [11], estimation of the propagation channels to/from the RIS elements [9], [12]–[15], as well as the use of this estimate to employ optimized configuration of the RIS elements [16], [17]. In radio localization, RISs can provide a strong and controllable non-line-of-sight (NLOS) signal path, as well as an extra location reference.

Many works have studied the benefits of RISs in radio localization through deriving Cramér-Rao lower bounds (CRB) and/or by designing estimation algorithms that use the reflected signal from the RIS to improve or enable UE localization [18]–[31]. In [18], the CRB on the location and orientation of the UE have been derived for a multiple-input multiple-output (MIMO) system equipped with an RIS, where considerable improvements in estimation accuracy have been observed because of the RIS. It has been shown that 3D localization is possible in an RIS-equipped SISO system [1], [20]. Furthermore, in [19], [30], SISO localization is performed with the help of a stripe-like RIS with blocked line-of-sight (LOS) path even when the path from RIS to UE is obstructed severely. Localization in the near-field of the RIS through analyzing the CRB has been studied in

Parts of this paper have been presented at the IEEE International Conference on Communications 2021 [1].

This work was supported, in part, by the Swedish Research Council under grant 2018-03701, the EU H2020 RISE-6G project under grant 101017011, Alice and Lars Erik Landahls fond under grant 90211117, Chalmers research fond under grant 90211102, the Spanish Ministry of Science and Innovation PID2020-118984GB-I00 and by the Catalan ICREA Academia Programme.

K. Keykhosravi, M.F. Keskin, and H. Wymeersch are with the Department of Electrical Engineering, Chalmers University of Technology, Gothenburg 41296, Sweden (e-mail: kamrank@chalmers.se); G. Seco-Granados is with the Department of Telecommunications and Systems Engineering, Universitat Autonòma de Barcelona, Spain; and Petar Popovski is with the Department of Electronic Systems, Aalborg University, Denmark.

[24] for infinite phase resolution and in [26] for limited one. Moreover, in [29], an uplink near-field localization algorithm is proposed for RIS-aided scenarios with LOS blockage. To estimate and counteract such blockages, a joint beam training and positioning method is developed in [31] in multi-RIS assisted mmWave communications.

Most of the aforementioned works consider quasi-static channels, where the movement of the UE during pilot transmission is negligible. While the effect of UE mobility has been unexplored in RIS-based localization literature, a number of works consider UE mobility for RIS-aided communication systems [32]–[40]. A continuous-time model for RIS-aided satellite communication has been derived in [32], where the movement of the satellite has been taken into consideration in optimization of the RIS phase shifts. Similarly, [39] investigates RIS phase shift design to simultaneously minimize the delay and Doppler spread and maximize the SNR in RIS-aided high-mobility vehicular communications under predictable UE mobility. In [33], it has been shown that the multipath fading effect caused by UE movement can be mitigated in an RIS-aided scenario. In [34], the authors presented a transmission protocol for channel estimation in a high-mobility scenario, where an intelligent *refracting* surface is mounted on the car. Following a similar approach, the study in [40] proposes a two-stage transmission protocol and channel/Doppler estimation method in high-mobility RIS-aided scenarios, complemented by the design of RIS phase shifts to mitigate the RIS-induced Doppler effect. Two channel estimation schemes for an RIS-aided communication system have been proposed in [35], considering Doppler effects. Moreover, the study in [36] models doubly-selective high-mobility Rician channels in RIS-aided unmanned aerial vehicle (UAV) communications by including the Doppler effect, and deals with minimum mean squared error (MMSE) channel estimation and RIS phase shift optimization. Furthermore, a deep reinforcement learning-based method is proposed in [37] to jointly design BS beamforming and RIS phase shifts for RIS-assisted mmWave high-speed railway networks.

The spatial-wideband (WB) effect refers to the change of an array's response (spatial steering vector) due to the change in frequency within the signal bandwidth [41], [42]. This can cause the beam-squint effect in far-field [43], [44] and the misfocus effect in near-field [45]. The spatial-WB effect has been studied for the case of massive MIMO (see e.g. [41], [43], [44]) and also recently for RISs [46]–[48]. In [41], the authors develop a spatial-WB channel model, and tailored a channel estimation algorithm based on it. In [43], the effects of beam-squint have been analyzed and compensated for in designing analog codebooks. A channel estimation algorithm for a spatial-WB RIS-aided communication system has been proposed in [47]. Several RIS phase shift designs have been proposed in [48] to maximize information rate in the presence of the beam-squint effect. To the best of our knowledge, the combined contribution of UE mobility and spatial-WB effect have not yet been studied in the context of RIS-localization.

This paper extends our conference contribution in [1], where it was shown that in a SISO system equipped with a single RIS, 3D UE localization and synchronization is possible. In this paper, we define and study the problem of RIS-aided SISO localization under spatial-WB effects and user mobility. The main contributions of this paper can be summarized as follows.

- For the first time in the literature, we investigate the problem of single-snapshot RIS-aided SISO 3D localization and synchronization under UE mobility and spatial-WB effects.
- We develop a geometric channel model for orthogonal frequency-division multiplexing (OFDM) signal propagation under the far-field assumption, by explicitly taking into account UE mobility and spatial-WB effects. Unlike the studies on RIS-aided communications with UE mobility [32]–[40], the developed model formulates the LOS (i.e., BS-to-UE) and NLOS (i.e., BS-to-RIS-to-UE) channels as a function of individual geometric parameters consisting of delays, Doppler shifts, and angle-of-departures (AoDs) in azimuth and elevation. In addition, unlike the existing literature on RIS-aided localization [18]–[31], we incorporate Doppler shift into our model.
- We design a low-complexity algorithm for joint localization and synchronization of UE, accompanied by time-orthogonal RIS phase profile design to combat interpath interference. First, we estimate the channel gain, delay and Doppler of the LOS path, and subtract its effect from the received signal. Based on the resulting LOS-interference-eliminated signal, we then estimate the parameters of the NLOS path, involving the delay, Doppler and AoD from the RIS to UE. In the final stage, 3D position and clock bias of the UE are computed using the estimated geometric channel parameters. The proposed algorithm attains the theoretical bounds at high SNRs when the spatial-WB effects are negligible.
- We study the influence of UE mobility, spatial-WB effects, and the presence of scatterers on the estimation error through extensive simulation of the estimator and evaluation of the CRB, considering directional and random RIS phase profiles.

Our results suggest that in terms of fundamental bounds, neither UE mobility nor spatial-WB effects influence the estimation accuracy. However, in terms of the accuracy of the estimator (designed based on the spatial-narrowband (NB) model), the spatial-WB effects reduce the position accuracy for large sizes of the RIS and large bandwidths when the angle between the direction of arrival or departure and the RIS normal is large. The performance of our estimator is not affected by the UE speed.

*Organization:* The remainder of the paper is organized as follows. In Section II, we present the system setup and derive the channel model in Section III. The RIS phase profile design is presented in Section IV. The estimator is described in Section V through a number of separate algorithms. In Section VI, we calculate the estimation errors through simulation and compare them with the CRB for an example of system parameters. Finally, Section VII concludes the paper.

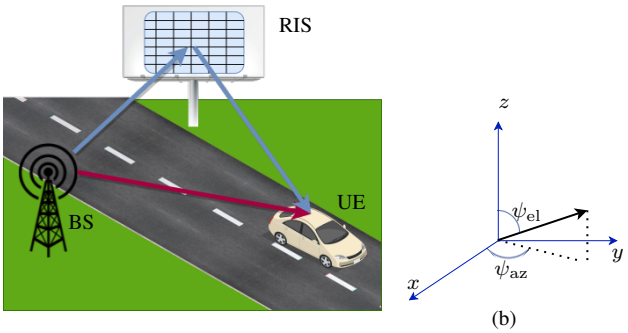


Fig. 1: (a): System setup, (b): Elevation and azimuth angles of a generic vector.

*Notation:* We represent vectors by bold-face lowercase letters (e.g., $\boldsymbol{x}$) and matrices by bold-face uppercase ones (e.g., $\boldsymbol{X}$). The $n$th element of the vector $\boldsymbol{x}$ is shown by $[\boldsymbol{x}]_n$ and with $[\boldsymbol{X}]_{m,n}$ we indicate the element on the $m$th row and the $n$th column of matrix $\boldsymbol{X}$. Furthermore, $[\boldsymbol{X}]_{:,n}$ ($[\boldsymbol{X}]_{n,:}$) denote the $n$th column (row) of matrix $\boldsymbol{X}$. The subindex $m:n$ indicates all the elements between (and including) $m$ and $n$. The Kronecker product is shown by $\otimes$ and the Hadamard product by $\odot$. The real and imaginary parts of the complex number $x$ are shown by $\Re(x)$ and $\Im(x)$, respectively. The matrix vectorization operator is indicated by $\text{vec}(\cdot)$. The vector $\mathbf{1}_L$ indicates the vector of length $L$, all of whose elements are one.

## II. System and Channel Model

### A. System setup

We consider a wireless system with a single-antenna transmitter, one RIS, and a single-antenna UE as shown in Fig. 1(a). We indicate the position of the BS and the RIS center by $\boldsymbol{p}_{\text{b}} \in \mathrm{R}^3$ and $\boldsymbol{p}_{\text{r}} \in \mathrm{R}^3$ according to some general coordinate system. The values of $\boldsymbol{p}_{\text{b}}$ and $\boldsymbol{p}_{\text{r}}$ as well as the orientation of the RIS are assumed to be known. Additionally, we assume that the UE is not time-synchronized to the BS, leading to an unknown clock bias $\Delta_t \in \mathrm{R}$ at the UE with respect to the BS. In addition to the UE's position ($\boldsymbol{p} \in \mathrm{R}^3$) and clock bias $\Delta_t$, its velocity ($\boldsymbol{v} \in \mathrm{R}^3$) is unknown and to be estimated. The RIS is a uniform planar array (UPA) with $M = M_1 \times M_2$ elements. The element in the $r$th row ($r \in \{0, \ldots, M_1 - 1\}$) and $s$th column ($s \in \{0, \ldots, M_2 - 1\}$) has the position $\boldsymbol{q}_{r,s} = [dr - d(M_1-1)/2), 0, ds - d(M_2-1)/2]$ in the local coordinate system of RIS, with $d$ being the spacing between the elements. The phase profile matrix of the RIS at time $\ell$ is shown by $\boldsymbol{\Gamma}_\ell \in \mathbb{C}^{M_1 \times M_2}$, where $[\boldsymbol{\Gamma}_\ell]_{r,s}$ indicates the phase shift applied to the impinging signal via the RIS element in the $r$th row and $s$th column.

### B. Geometric relations

We introduce $v_{\text{b}}$ and $v_{\text{r}}$ as the UE's radial velocity (Doppler) along UE-BS and UE-RIS directions, respectively, and are given by

$$v_{\text{b}} = \boldsymbol{v}^\top(\boldsymbol{p}_{\text{b}} - \boldsymbol{p})/\|\boldsymbol{p}_{\text{b}} - \boldsymbol{p}\| \tag{1}$$

$$v_{\text{r}} = \boldsymbol{v}^\top(\boldsymbol{p}_{\text{r}} - \boldsymbol{p})/\|\boldsymbol{p}_{\text{r}} - \boldsymbol{p}\|. \tag{2}$$

In addition, $\tau_{\text{b}}$ and $\tau_{\text{r}}$ represent, respectively, the delays of the direct and the reflected paths

$$\tau_{\text{b}} = \frac{\|\boldsymbol{p}_{\text{b}} - \boldsymbol{p}\|}{c} + \Delta_t \tag{3}$$

$$\tau_{\text{r}} = \frac{\|\boldsymbol{p}_{\text{b}} - \boldsymbol{p}_{\text{r}}\| + \|\boldsymbol{p}_{\text{r}} - \boldsymbol{p}\|}{c} + \Delta_t, \tag{4}$$

where $\Delta_t$ is the clock bias and $c$ is the light speed. The AoD from the RIS to the UE is indicated by $\boldsymbol{\phi}$, which corresponds to the direction of the vector $\boldsymbol{s}$ from the RIS to the UE in the local coordinate system of the RIS, i.e., $\boldsymbol{s} = \boldsymbol{R}(\boldsymbol{p} - \boldsymbol{p}_{\text{r}})$, where $\boldsymbol{R}$ is a rotation matrix that maps the global frame of reference to the RIS local coordinate system. More specifically, we have

$$[\boldsymbol{\phi}]_{\text{az}} = \text{atan2}\left([\boldsymbol{s}]_2, [\boldsymbol{s}]_1\right) \tag{5}$$

$$[\boldsymbol{\phi}]_{\text{el}} = \arccos\left(\frac{[\boldsymbol{s}]_3}{\|\boldsymbol{p} - \boldsymbol{p}_{\text{r}}\|}\right). \tag{6}$$

### C. Signal and baseline channel model

We consider the transmission of $L$ OFDM symbols with $N$ subcarriers. Under the assumption of perfect frequency synchronization between the UE and the BS, the received signal after the fast Fourier transform (FFT) operation at the UE in the frequency/slow-time domain can be represented by the matrix $\boldsymbol{Y} \in \mathbb{C}^{N \times L}$ as

$$\boldsymbol{Y} = \boldsymbol{Y}_{\text{b}} + \boldsymbol{Y}_{\text{r}} + \boldsymbol{N}, \tag{7}$$

where the noise matrix is represented with $\boldsymbol{N}$, whose elements are drawn independently from a circularly symmetric Gaussian distribution with variance $N_0$. The matrices $\boldsymbol{Y}_{\text{b}}$ and $\boldsymbol{Y}_{\text{r}}$ describe the signal received through the direct and reflected path, respectively. As a baseline, we consider a channel model that ignores any spatial-WB effect and assumes a sufficiently short observation time such that approximately $\boldsymbol{v} = \boldsymbol{0}$. For simplicity, we assume that all the transmitted symbols are equal to one. Hence following [1]

$$\boldsymbol{Y}_{\text{b}} = g_{\text{b}}\boldsymbol{D}(\tau_{\text{b}}) \tag{8}$$

$$\boldsymbol{Y}_{\text{r}} = g_{\text{r}}\boldsymbol{D}(\tau_{\text{r}}) \odot \boldsymbol{A}(\boldsymbol{\phi}), \tag{9}$$

where the complex channel gain for the direct path is indicated by $g_{\text{b}}$ and for the reflected one by $g_{\text{r}}$. The matrix $\boldsymbol{D} \in \mathbb{C}^{N \times L}$ is the delay steering vector repeated across time and is defined as

$$\boldsymbol{D}(\tau) = [1, e^{-\jmath 2\pi \Delta_f \tau}, \ldots, e^{-\jmath 2\pi (N-1)\Delta_f \tau}]^\top \mathbf{1}_L^\top, \tag{10}$$

where $\Delta_f$ is the subcarrier spacing. Let $\boldsymbol{\theta}$ denote the known angle-of-arrival (AoA) from the BS to the RIS. In (9), $\boldsymbol{A}(\boldsymbol{\phi}) \in \mathbb{C}^{N \times L}$ captures the effects of RIS phase modulation, given by

$$[\boldsymbol{A}(\boldsymbol{\phi})]_{n,\ell} = \boldsymbol{a}(\boldsymbol{\theta})^\top \text{diag}(\boldsymbol{\gamma}_\ell)\boldsymbol{a}(\boldsymbol{\phi}), \tag{11}$$

where all the rows of $\boldsymbol{A}(\boldsymbol{\phi})$ are identical. The vector $\boldsymbol{\gamma}_\ell \in \mathrm{C}^M$ is defined as

$$\boldsymbol{\gamma}_\ell = \text{vec}(\boldsymbol{\Gamma}_\ell) \tag{12}$$

and it represents the RIS phase profile vector at time $\ell$. The vector $\boldsymbol{a}(\cdot) \in \mathbb{C}^M$ is the narrowband RIS response steering vector and is defined as

$$[\boldsymbol{a}(\boldsymbol{\psi})]_m = \exp\left(\jmath \boldsymbol{k}(\boldsymbol{\psi})^\top [\boldsymbol{Q}]_{:,m}\right), \tag{13}$$

where the relative RIS element positions are contained in

$$\boldsymbol{Q} = [\boldsymbol{q}_{0,0}, \boldsymbol{q}_{1,0}, \ldots, \boldsymbol{q}_{M_1-1,M_2-1}]. \tag{14}$$

The wavenumber vector is defined as

$$\boldsymbol{k}(\boldsymbol{\psi}) = \frac{2\pi}{\lambda}[\sin([\boldsymbol{\psi}]_{\rm el})\cos([\boldsymbol{\psi}]_{\rm az}), \sin([\boldsymbol{\psi}]_{\rm el})\sin([\boldsymbol{\psi}]_{\rm az}), \cos([\boldsymbol{\psi}]_{\rm el})]^\top, \tag{15}$$

where $[\boldsymbol{\psi}]_{\rm az}$ and $[\boldsymbol{\psi}]_{\rm el}$ represent the azimuth and elevation of the generic direction described by angle $\boldsymbol{\psi}$ (see Fig. 1(b)), and $\lambda = c/f_c$ is the wavelength at the carrier frequency.

## III. Extended channel models for spatial-WB and UE mobility

While the channel model from Section II-C is common in the RIS literature, it is limited in two ways. First of all, when the RIS and the signal bandwidth are both large, the model fails to capture the variation of the RIS steering vector with the frequency, which is a consequence of the definition of the structure of $\boldsymbol{A}(\boldsymbol{\phi})$ with identical rows. Secondly, the assumption of negligible velocity severely limits the duration of the coherent processing interval $L/\Delta_f$.

We now present two channel models that extend the model from Section II-C in non-trivial ways: the first model captures both the spatial-WB effects [46]–[48] and UE mobility [35], and it is used for developing the CRB and simulating the channel; the second model neglects the spatial-WB effects and is employed in the estimator design. The original model (8)–(9), which neglects both UE mobility and spatial-WB effects, will be assumed for designing the RIS phase profiles.

### A. Signal transmission: Dynamic spatial-wideband model

In the dynamic spatial-WB model, two fundamental changes occur with respect to the static spatial-NB model in (8)–(9). First, the RIS response matrix $\boldsymbol{A}(\boldsymbol{\phi})$ in (11) becomes frequency-dependent, leading to non-identical rows. Second, we incorporate new steering matrices that capture fast-time (sample-level) and slow-time (symbol-level) Doppler-induced phase progressions. Accordingly, as shown in Appendix A, (8)–(9) should be extended to[1]

$$\boldsymbol{Y}_{\rm b} = g_{\rm b}\boldsymbol{F}\boldsymbol{E}(v_{\rm b})\boldsymbol{F}^{\rm H}\left(\boldsymbol{D}(\tau_{\rm b}) \odot \boldsymbol{C}_{\rm w}(v_{\rm b})\right), \tag{16}$$

$$\boldsymbol{Y}_{\rm r} = g_{\rm r}\boldsymbol{F}\boldsymbol{E}(v_{\rm r})\boldsymbol{F}^{\rm H}\left[\boldsymbol{D}(\tau_{\rm r}) \odot \boldsymbol{A}_{\rm w}(\boldsymbol{\phi}) \odot \boldsymbol{C}_{\rm w}(v_{\rm r})\right]. \tag{17}$$

Here, the matrix $\boldsymbol{F} \in \mathbb{C}^{N\times N}$ is the unitary DFT matrix with elements

$$[\boldsymbol{F}]_{n,\ell} = \frac{1}{\sqrt{N}} e^{-\jmath 2\pi \frac{n\ell}{N}} \tag{18}$$

for $n, \ell \in \{0, \ldots, N-1\}$. In addition, $\boldsymbol{A}_{\rm w}(\boldsymbol{\phi})$ represents the spatial-wideband version of $\boldsymbol{A}(\boldsymbol{\phi})$ in (11); namely,

$$[\boldsymbol{A}_{\rm w}(\boldsymbol{\phi})]_{n,\ell} = \boldsymbol{a}_n(\boldsymbol{\theta})^\top \mathrm{diag}(\boldsymbol{\gamma}_\ell)\boldsymbol{a}_n(\boldsymbol{\phi}), \tag{19}$$

where the RIS steering vector now depends on the subcarrier index $n$:

$$[\boldsymbol{a}_n(\boldsymbol{\psi})]_m = \exp\left(\jmath \boldsymbol{k}_n(\boldsymbol{\psi})^\top [\boldsymbol{Q}]_{:,m}\right), \tag{20}$$

with $\boldsymbol{k}_n(\boldsymbol{\psi})$ being defined as in (15) by replacing $\lambda$ with

$$\lambda_n = \frac{c}{f_c + n\Delta_f}. \tag{21}$$

Moreover, the effects of UE mobility on the received signal is captured by the inter-carrier interference (ICI) phase rotation matrix $\boldsymbol{E}(v) \in \mathbb{C}^{N\times N}$, which models Doppler-induced *fast-time* phase rotations within an OFDM symbol [49]–[51], and the temporal steering matrix $\boldsymbol{C}_{\rm w}(v) \in \mathbb{C}^{N\times L}$, which quantifies Doppler-induced *slow-time* phase progressions across consecutive OFDM symbols [52], [53]:

$$[\boldsymbol{C}_{\rm w}(v)]_{n,\ell} \triangleq e^{\jmath 2\pi \ell T_{\rm sym} v/\lambda_n} \tag{22}$$

$$\boldsymbol{E}(v) \triangleq \mathrm{diag}\left(1, e^{\jmath 2\pi \frac{T_{\rm o}}{N} v/\lambda}, \ldots, e^{\jmath 2\pi \frac{T_{\rm o}(N-1)}{N} v/\lambda}\right) \tag{23}$$

for $n \in \{0, \ldots, N-1\}$ and $\ell \in \{0, \ldots, L-1\}$. Here, $T_{\rm o} = 1/\Delta_f$ is the elementary symbol duration and $T_{\rm sym} = T_{\rm cp} + T_{\rm o}$ is the total signal duration, with $T_{\rm cp}$ denoting the cyclic prefix (CP) duration.

### B. Signal transmission: Dynamic spatial-narrowband model

In order to reduce the complexity of our estimator, we design it based on a simpler channel than (16)–(17) by assuming a spatial-narrowband model. In this case, the channel in (16)–(17) is constructed by reverting $\lambda_n$ in (21) back to $\lambda = c/f_c$. This will simplify the structure of matrices $\boldsymbol{C}_{\rm w}$ and $\boldsymbol{A}_{\rm w}$ by making their elements independent of the subcarrier index $n$, i.e., all of their rows become identical. Specifically, under the spatial-narrowband model, the received signal in (16)–(17) specializes to

$$\boldsymbol{Y}_{\rm b} = g_{\rm b}\boldsymbol{F}\boldsymbol{E}(v_{\rm b})\boldsymbol{F}^{\rm H}\left(\boldsymbol{D}(\tau_{\rm b}) \odot \boldsymbol{C}(v_{\rm b})\right) \tag{24}$$

$$\boldsymbol{Y}_{\rm r} = g_{\rm r}\boldsymbol{F}\boldsymbol{E}(v_{\rm r})\boldsymbol{F}^{\rm H}\left[\boldsymbol{D}(\tau_{\rm r}) \odot \boldsymbol{A}(\boldsymbol{\phi}) \odot \boldsymbol{C}(v_{\rm r})\right], \tag{25}$$

where the subcarrier-dependent matrices $\boldsymbol{C}_{\rm w}(v)$ and $\boldsymbol{A}_{\rm w}(\boldsymbol{\phi})$ in (16)–(17) revert to their narrowband (subcarrier-independent) counterparts $\boldsymbol{C}(v)$ and $\boldsymbol{A}(\boldsymbol{\phi})$. Here, $\boldsymbol{A}(\boldsymbol{\phi})$ is defined in (11) and[2]

$$[\boldsymbol{C}(v)]_{n,\ell} \triangleq e^{\jmath 2\pi \ell T_{\rm sym} v/\lambda}. \tag{26}$$

For the spatial-narrowband approximation in (24) and (25) to be valid, the following conditions must be satisfied (see Appendix B for details):

$$\max\{v_{\rm r}, v_{\rm b}\} L T_{\rm sym} B \approx \max\{v_{\rm r}, v_{\rm b}\} L N \ll c \tag{27}$$

$$\max(M_1, M_2) d \sin(\alpha) B \ll c, \tag{28}$$

which ensure the validity of the approximations $\boldsymbol{C}_{\rm w}(v) \approx \boldsymbol{C}(v)$ and $\boldsymbol{A}_{\rm w}(\boldsymbol{\phi}) \approx \boldsymbol{A}(\boldsymbol{\phi})$, respectively. Here, $\alpha =$

[1] We assume that the angular displacement caused by UE mobility is negligible due to the far-field assumption.

[2] Note that the dynamic spatial-narrowband model (24)–(25) reverts to the static spatial-narrowband model (8)–(9) when $v = 0$.

$\max\{\alpha_\phi, \alpha_\theta\}$, where $\alpha_\phi$ and $\alpha_\theta$ are the angles between the RIS normal ($[0,1,0]^\top$) and the two vectors $\boldsymbol{k}(\boldsymbol{\phi})$ and $\boldsymbol{k}(\boldsymbol{\theta})$, respectively, which are defined in (15). While the condition in (27) almost always holds (corresponding to the assumption of small time-bandwidth product [52]), the condition in (28) does not hold for RISs with large dimension combined with signals of large bandwidth [41]. We will study the effects of this assumption in Section VI.

## IV. RIS PHASE PROFILE DESIGN

In this section, we consider the design of the RIS phase profile $\boldsymbol{\Gamma}_\ell$ for $\ell = 0, \dots L-1$. In order to mitigate the interference between the direct path and the reflected one, we use the method described in [54]. The method deploys temporal orthogonal RIS phase profiles and a post processing at the receiver. This process resembles the code-division multiplexing, which is a well-known method in wireless communications (see e.g., [55]). It can remove the interpath interference completely in the static scenario ($\boldsymbol{v} = \boldsymbol{0}$). Next, we use the static channel model in Section II-C to describe the RIS phase profile design.

### A. Orthogonal RIS phase profiles

We set $L$ to be an even number and for each $k = 0, 1, \dots, L/2$ we select beams $\boldsymbol{B}_k \in \mathbb{C}^{M_1 \times M_2}$ either randomly or according to a directional codebook (we elaborate on this in Section IV-C). Also, similarly as in (12), we define $\boldsymbol{b}_k = \mathrm{vec}(\boldsymbol{B}_k)$. Then we set $\boldsymbol{\gamma}_{2k} = \boldsymbol{b}_k$ and $\boldsymbol{\gamma}_{2k+1} = -\boldsymbol{b}_k$. By doing so, from (11) we have that $[\boldsymbol{A}(\boldsymbol{\phi})]_{:,2k+1} = -[\boldsymbol{A}(\boldsymbol{\phi})]_{:,2k}$. Therefore, from (8) and (9), we have

$$
\begin{aligned}
[\boldsymbol{Y}_\mathrm{b}]_{:,2k+1} &= g_b \left[\boldsymbol{D}(\tau_\mathrm{b})\right]_{:,2k+1} && (29)\\
&= [\boldsymbol{Y}_\mathrm{b}]_{:,2k} && (30)\\
[\boldsymbol{Y}_\mathrm{r}]_{:,2k+1} &= g_\mathrm{r} \left[\boldsymbol{D}(\tau_\mathrm{r})\right]_{:,2k+1} \odot [\boldsymbol{A}(\boldsymbol{\phi})]_{:,2k+1} && (31)\\
&= -g_\mathrm{r} \left[\boldsymbol{D}(\tau_\mathrm{r})\right]_{:,2k} \odot [\boldsymbol{A}(\boldsymbol{\phi})]_{:,2k} && (32)\\
&= -[\boldsymbol{Y}_\mathrm{r}]_{:,2k}. && (33)
\end{aligned}
$$

The post-processing step at the receiver involves calculating matrices $\boldsymbol{Z}_\mathrm{b} \in \mathbb{C}^{N \times L/2}$ and $\boldsymbol{Z}_\mathrm{r} \in \mathbb{C}^{N \times L/2}$ as

$$
\begin{aligned}
[\boldsymbol{Z}_\mathrm{b}]_{:,k} &= [\boldsymbol{Y}]_{:,2k} + [\boldsymbol{Y}]_{:,2k+1} && (34)\\
&= 2g_\mathrm{b} \left[\boldsymbol{D}(\tau_\mathrm{b})\right]_{:,2k} + [\boldsymbol{N}]_{:,2k} + [\boldsymbol{N}]_{:,2k+1} && (35)\\
&= 2[\boldsymbol{Y}_\mathrm{b}]_{:,2k} + [\boldsymbol{N}]_{:,2k} + [\boldsymbol{N}]_{:,2k+1} && (36)\\
[\boldsymbol{Z}_\mathrm{r}]_{:,k} &= [\boldsymbol{Y}]_{:,2k} - [\boldsymbol{Y}]_{:,2k+1} && (37)\\
&= 2g_\mathrm{r} \left[\boldsymbol{D}(\tau_\mathrm{r})\right]_{:,2k} \odot [\boldsymbol{A}(\boldsymbol{\phi})]_{:,2k} + [\boldsymbol{N}]_{:,2k} - [\boldsymbol{N}]_{:,2k+1}\\
&= 2[\boldsymbol{Y}_\mathrm{r}]_{:,2k} + [\boldsymbol{N}]_{:,2k} - [\boldsymbol{N}]_{:,2k+1}. && (38)
\end{aligned}
$$

It can be seen from (36) and (38) that the matrix $\boldsymbol{Y}_\mathrm{b}$ ($\boldsymbol{Y}_\mathrm{r}$) depends only on the parameters of the direct (reflected) channel. Therefore, with the aforementioned RIS phase profile design and post-processing, we can remove the interference between the two paths, which facilitates the estimation of the channel parameters. Furthermore, from (36) and (38) it can be seen the signals $\boldsymbol{Z}_\mathrm{b}$ and $\boldsymbol{Z}_\mathrm{r}$ have higher SNRs compared to the signals $\boldsymbol{Y}_\mathrm{b}$ and $\boldsymbol{Y}_\mathrm{r}$, respectively. This indicates that the presented orthogonal coding does not result in a waste of resources by repeating the beams. For clarification, we consider a toy example with $L = 4$ and $M = 1$ and $[\boldsymbol{b}_0, \boldsymbol{b}_1] = [e^{\jmath\theta_0}, e^{\jmath\theta_1}]$ for some $\theta_0, \theta_1 \in [0\, 2\pi)$. Then the set of RIS phase profiles would be $[\boldsymbol{\gamma}_0, \boldsymbol{\gamma}_1, \boldsymbol{\gamma}_2, \boldsymbol{\gamma}_3] = [e^{\jmath\theta_0}, -e^{\jmath\theta_0}, e^{\jmath\theta_1}, -e^{\jmath\theta_1}]$. Also if the noise is neglected, we have $[\boldsymbol{Z}_\mathrm{b}]_{:,k} = 2g_\mathrm{b}\boldsymbol{d}(\tau_\mathrm{b})$ and $[\boldsymbol{Z}_\mathrm{r}]_{:,k} = 2g_\mathrm{r}e^{\jmath\theta_k}\boldsymbol{d}(\tau_\mathrm{r})$ for $k = 0, 1$.

For future use, we refer to the post processing step in (36) and (38) as matching the signal $\boldsymbol{Y}$ with vectors $\boldsymbol{w}_\mathrm{b} = [1,1]^\top$ and $\boldsymbol{w}_\mathrm{r} = [1,-1]^\top$, respectively. We explain this step in Algorithm 1 as follows.

**Algorithm 1** *match($\boldsymbol{Y}$,$\boldsymbol{w}$)*

**Inputs:** Received signal ($\boldsymbol{Y} \in \mathbb{C}^{N \times L}$) and vector $\boldsymbol{w} \in \mathbb{C}^2$.
**Output:** $\boldsymbol{Z} \in \mathbb{C}^{N \times L/2}$.

1: **for** $k \in \{0, \dots, L/2-1\}$ **do**
2: $\quad [\boldsymbol{Z}]_{:,k} = [\boldsymbol{w}]_1 [\boldsymbol{Y}]_{:,2k} + [\boldsymbol{w}]_2 [\boldsymbol{Y}]_{:,2k+1}$
**return** $\boldsymbol{Z}$

### B. Loss of orthogonality due to UE mobility

For the dynamic case ($\boldsymbol{v} \neq \boldsymbol{0}$), one can write (36)–(38) as

$$
\begin{aligned}
[\boldsymbol{Z}_\mathrm{b}]_{:,k} &= (2 - \epsilon(v_\mathrm{b}))[\boldsymbol{Y}_\mathrm{b}]_{:,2k} + \epsilon(v_\mathrm{r})[\boldsymbol{Y}_\mathrm{r}]_{:,2k}\\
&\quad + [\boldsymbol{N}]_{:,2k} + [\boldsymbol{N}]_{:,2k+1} && (39)\\
[\boldsymbol{Z}_\mathrm{r}]_{:,k} &= (2 - \epsilon(v_\mathrm{r}))[\boldsymbol{Y}_\mathrm{r}]_{:,2k} + \epsilon(v_\mathrm{b})[\boldsymbol{Y}_\mathrm{b}]_{:,2k}\\
&\quad + [\boldsymbol{N}]_{:,2k} - [\boldsymbol{N}]_{:,2k+1}, && (40)
\end{aligned}
$$

where $\epsilon(v) = 1 - \exp(\jmath 2\pi T_\mathrm{sym} v/\lambda)$. By comparing (39)–(40) with (36)–(38), one can see that UE mobility introduces two impairments to the proposed method:

- Energy loss: some of the signal energy of the desired path is lost since $|2 - \epsilon(v)| < 2$
- Residual interference: the second term in (39)–(40) exhibits the interference from the undesired path.

We design our estimator based on the approximation $\epsilon(v) = 0$. To counter the aforementioned impairments, we apply multiple iterations and deploy successive cancellation.

### C. RIS phase profile design

In this section, we discuss the selection of $\boldsymbol{B}_k$ or equivalently $\boldsymbol{b}_k$. We consider two methods, namely random and directional profiles. The latter can be used when a prior information about the UE location is available and the former when such information is lacking.

*1) Random profile:* With the random codebook, for $m = 0, \dots, M-1$ and $k = 0, \dots, L/2-1$ we let

$$[\boldsymbol{b}_k]_m = e^{\jmath\theta_{k,m}}, \qquad (41)$$

where $\theta_{k,m}$ are independent and identically distributed (iid) realizations of the uniform distribution over the interval $[0, 2\pi)$.

*2) Directional profile:* Here, we assume that we have a prior knowledge of the UE position, $\boldsymbol{\xi}$, which is distributed uniformly throughout the sphere

$$|\boldsymbol{p} - \boldsymbol{\xi}| < \sigma. \qquad (42)$$

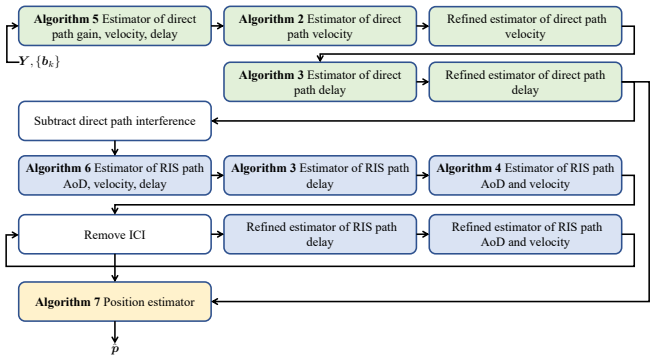


Fig. 2: A flowchart of Algorithm 8, comprising three stages: estimation of the parameters of the direct path (green), estimation of the parameters of the reflected path (blue), and position estimation (orange).

We call $\sigma$ the uncertainty radius. Given the prior position knowledge $\boldsymbol{\xi}$, the RIS phase profile is designed as follows. We first select $L/2$ points $\boldsymbol{\xi}_0, \ldots, \boldsymbol{\xi}_{L/2-1}$ randomly (with uniform distribution) from the sphere centered at $\boldsymbol{\xi}$ with radius $\sigma$. Second, we set $\boldsymbol{b}_k = \boldsymbol{f}(\boldsymbol{\xi}_k)$ where for $m = 0, \ldots, M-1$:

$$[\boldsymbol{f}(\boldsymbol{x})]_m = \exp\left(-\jmath\left(\boldsymbol{k}(\boldsymbol{\theta})^\top + \frac{2\pi(\boldsymbol{x}^\top - \boldsymbol{p}_{\mathrm{r}}^\top)}{\lambda\|\boldsymbol{x}-\boldsymbol{p}_{\mathrm{r}}\|}\right)[\boldsymbol{Q}]_m\right). \tag{43}$$

One can see that with the phase profile in (43) the reflected signal energy from the RIS is concentrated towards the point $\boldsymbol{x}$.

## V. Estimation Algorithm

In this section, we propose an estimator to estimate first the channel parameters and then the UE position and clock bias based on them. The overall process is described in the flowchart of Fig. 2 using multiple separate procedures described in Algorithm 2–7 as building blocks. To estimate the parameters, we first obtain a coarse estimation and then use it as an initial point in a refinement process, which is a standard approach in localization literature (see e.g., [4]). Next we describe the Algorithms using a bottom-up approach.

### A. Estimation of $v_{\mathrm{b}}$

For estimating the UE velocity, we first obtain a coarse estimation using standard methods based on the discrete Fourier transform (DFT) matrix and then provide a refined estimation by using the coarse estimate as the initial point for our optimization.

Algorithm 2 provides a coarse estimation of the velocity. The input signal is an estimate of $\boldsymbol{Z}_{\mathrm{b}} = \mathit{match}(\boldsymbol{Y}, \boldsymbol{w}_{\mathrm{b}})$ described in (39). One can see that for every $n$ we have that

$$[\boldsymbol{Z}_{\mathrm{b}}]_{n,:} \approx \xi_n[1, e^{\jmath 2h_{\mathrm{v}}v_{\mathrm{b}}}, e^{\jmath 4h_{\mathrm{v}}v_{\mathrm{b}}}, \ldots, e^{\jmath(L-2)h_{\mathrm{v}}v_{\mathrm{b}}}] \tag{44}$$

for some scalar $\xi_n \in \mathbb{C}$, where $h_{\mathrm{v}} = 2\pi T_{\mathrm{sym}}/\lambda$. Then it can be seen that the maximum of

$$f(v) = \|\hat{\boldsymbol{Z}}_{\mathrm{b}}[1, e^{\jmath 2h_{\mathrm{v}}v}, \ldots, e^{\jmath(L-2)h_{\mathrm{v}}v}]^{\mathrm{H}}\|^2 \tag{45}$$

provides an estimate of $v_{\mathrm{b}}$. To find the maximum of $f(v)$, we note that the structure shown in (44) is similar to the rows of the DFT matrix $\boldsymbol{F}$ in Line 1 of Algorithm 2, that is

$$[\boldsymbol{F}]_{n,:} = \frac{\sqrt{2}}{\sqrt{L}}[1, e^{-\jmath\omega n}, e^{-\jmath 2\omega n}, \ldots, e^{-\jmath(L/2-1)\omega n}] \tag{46}$$

for all $n = 0, \ldots, N_{\mathrm{v}} - 1$. Here, $\omega = 2\pi/N_{\mathrm{v}}$ and $N_{\mathrm{v}}$ is a design parameter that determines the dimension of the DFT matrix and accuracy of our coarse estimation. By comparing (46) to (44), one can approximate the $\arg\max_v f(v)$ via the maximization in Line 3 and the assignment in Line 6. Finally, the condition in Line 4 compensates for the wrap-around effect in the complex-exponential function when $v_{\mathrm{b}} < 0$.

*Refinement*: Let the output of the Algorithm 2 be $v_0$. To refine this estimation, we perform the maximization $\hat{v}_b = \max_v f(v)$ via a *quasi-Newton* algorithm initiated at $v_0$.

**Algorithm 2** *Coarse_Velocity_Est($\hat{\boldsymbol{Z}}_{\mathrm{b}}$)*

**Inputs:** Signal ($\hat{\boldsymbol{Z}}_{\mathrm{b}} \in \mathbb{C}^{N\times L/2}$)
**Parameters:** DFT dimension ($N_{\mathrm{v}}$)
**Output:** $\hat{v}_0$

1: $\boldsymbol{F} \leftarrow N_{\mathrm{v}} \times L/2$ DFT matrix
2: $\boldsymbol{Z}_{\mathrm{v}} \leftarrow \boldsymbol{F}\hat{\boldsymbol{Z}}_{\mathrm{b}}^\top$
3: $i_{\mathrm{m}} \leftarrow \mathrm{argmax}_i \|[\boldsymbol{Z}_{\mathrm{v}}]_{i,:}\|$
4: **if** $i_{\mathrm{m}} > N_{\mathrm{v}}/2$ **then**
5: $\quad i_{\mathrm{m}} \leftarrow i_{\mathrm{m}} - N_{\mathrm{v}} + 1$
6: $\hat{v}_0 \leftarrow i_{\mathrm{m}}\lambda/(2T_{\mathrm{sym}}N_{\mathrm{v}})$
7: **return** $\hat{v}_0$

### B. Estimation of ToA

Similar to Section V-A, the estimation of time-of-arrival (ToA) comprises coarse and fine estimation steps.

Algorithm 3 describes the coarse estimation of the ToA given the input signal $\boldsymbol{Z}_\tau$[3]. We assume that the columns of the input signal have the structure

$$[\boldsymbol{Z}_\tau]_{:,t} \approx \xi_t[1, e^{\jmath h_\tau \tau_{\mathrm{x}}}, \ldots, e^{\jmath(N-1)h_\tau\tau_{\mathrm{x}}}]^{\mathrm{H}} \tag{47}$$

for some $\xi_t \in \mathbb{C}$, where $\tau_{\mathrm{x}}$ represents either $\{\tau_{\mathrm{b}}$ or $\tau_{\mathrm{r}}\}$. Algorithm 3 can be explained similarly as in Section V-A using (47).

*Refinement:* Based on (47) a fine estimation of $\tau_{\mathrm{b}}$ or $\tau_{\mathrm{r}}$ can be found by calculating

$$\hat{\tau} = \arg\max_\tau \|[1, e^{\jmath h_\tau \tau}, \ldots, e^{\jmath(N-1)h_\tau\tau}]\boldsymbol{Z}_\tau\|^2, \tag{48}$$

where $h_\tau \leftarrow 2\pi\Delta_f$. The optimization (48) can be solved via a quasi-Newton algorithm that uses the coarse estimation as the initial point of search.

[3]We use Algorithm 3 within Algorithm 5, where the input ($\boldsymbol{Z}_\tau$) is an estimate of $\sum_t[\boldsymbol{Z}_{\mathrm{b}}]_{:,t}$ with dimension $N \times 1$ and also in Algorithm 6, where the input is an estimate of $\boldsymbol{Z}_{\mathrm{r}}$ with dimension $N \times L/2$.

**Algorithm 3** *Coarse_delay_Est($\boldsymbol{Z}_\tau$)*

**Inputs:** Signal ($\boldsymbol{Z}_\tau \in \mathbb{C}^{N\times T}$, where $T \in \{1, L/2\}$)
**Parameters:** IDFT dimension ($N_\tau$)
**Output:** $\hat{\tau}$

1: $\boldsymbol{F} \leftarrow N_\tau \times N$ DFT matrix
2: $\boldsymbol{W}_\tau \leftarrow \boldsymbol{F}^{\mathrm{H}} \boldsymbol{Z}_\tau$
3: $i_{\mathrm{m}} \leftarrow \mathrm{argmax}_i \|[\boldsymbol{W}_\tau]_{i,:}\|$
4: $\hat{\tau} \leftarrow i_{\mathrm{m}}/(\Delta_f N_\tau)$
5: **return** $\hat{\tau}$

### C. Joint estimation of velocity and AoD for the reflected path

In this section, we describe coarse and fine steps for joint estimation of the angle and velocity.

Algorithm 4 describes the coarse estimation process of AoD and velocity. We assume that the input signal $\boldsymbol{z}_\phi$ is proportional to the rows of the matrix $\boldsymbol{C}(v) \odot \boldsymbol{A}(\boldsymbol{\phi})$ and therefore has the structure

$$[\boldsymbol{z}_\phi]_k = \xi e^{\jmath 2k h_{\mathrm{v}} v} \boldsymbol{a}(\boldsymbol{\theta})^\top \mathrm{diag}(\boldsymbol{b}_k) \boldsymbol{a}(\boldsymbol{\phi}) \tag{49}$$

for some constant $\xi \in \mathbb{C}$ and velocity $v$, which is to be estimated. Also, the constant $h_{\mathrm{v}}$ is defined as $h_{\mathrm{v}} = 2\pi T_{\mathrm{sym}}/\lambda$.

To obtain a coarse estimation of $v$ and $\boldsymbol{\phi}$ based on the input signal $\boldsymbol{z}_\phi$ described in (49), Algorithm 4 uses a set of candidate AoDs. For the $s$th candidate, we calculate $\boldsymbol{z}_s$ in Line 4 and then normalize it in Line 5 to obtain $\boldsymbol{w}_s$. Assume that for some $s_{\mathrm{m}}$ we have $\boldsymbol{\phi}_{s_{\mathrm{m}}} = \boldsymbol{\phi}$, then we have that

$$\boldsymbol{z}_{\boldsymbol{\phi}} \propto [1, e^{\jmath 2h_{\mathrm{v}} v}, \ldots, e^{\jmath (L-2) h_{\mathrm{v}} v}]^\top \odot \boldsymbol{w}_{s_{\mathrm{m}}}. \tag{50}$$

Motivated by the structure in (50), we compute the correlation of $\boldsymbol{z}_{\boldsymbol{\phi}}$ with all $\boldsymbol{w}_s$ and all of the rows of the DFT matrix in Lines 6–7. Then, we search over different values of $s$ and $i$ (which indicates the rows of the DFT matrix) to find the one with the highest correlation in Line 8. We estimate $v_{\mathrm{r}}$ through Lines 10–12, which are the same steps as in Lines 4–6 of Algorithm 2. We explain in Appendix C how to choose the candidate AoDs.

*Refinement:* According to the right hand side (RHS) of (49), for $k \in \{0, \ldots, L/2\}$, we define

$$[\boldsymbol{g}(v, \boldsymbol{\phi})]_k = e^{\jmath 2k h_{\mathrm{v}} v} \boldsymbol{a}(\boldsymbol{\theta})^\top \mathrm{diag}(\boldsymbol{b}_k) \boldsymbol{a}(\boldsymbol{\phi}), \tag{51}$$

which is a function of $v$ and $\boldsymbol{\phi}$. Then one can estimate the constant $\xi$ as

$$\hat{\xi} = \boldsymbol{g}(v, \boldsymbol{\phi})^{\mathrm{H}} \boldsymbol{z}_\phi / \boldsymbol{g}(v, \boldsymbol{\phi})^{\mathrm{H}} \boldsymbol{g}(v, \boldsymbol{\phi}). \tag{52}$$

Next, we can define the objective function

$$f(v, \boldsymbol{\phi}) = \|\boldsymbol{z}_\phi - \left(\boldsymbol{g}(v, \boldsymbol{\phi})^{\mathrm{H}} \boldsymbol{z}_\phi / \boldsymbol{g}(v, \boldsymbol{\phi})^{\mathrm{H}} \boldsymbol{g}(v, \boldsymbol{\phi})\right) \boldsymbol{g}(v, \boldsymbol{\phi})\|. \tag{53}$$

To refine the estimation of $v$ and $\boldsymbol{\phi}$, we conduct two consecutive minimization of $f(v, \boldsymbol{\phi})$ via a quasi-Newton algorithm initiating at the coarse estimations.

**Algorithm 4** *Coarse_Velocity_Angle_Est($\boldsymbol{z}_\phi, \{\boldsymbol{b}_k\}$)*

**Inputs:** Signal ($\boldsymbol{z}_\phi \in \mathbb{C}^{L/2}$)
**Parameters:** DFT dimensions ($N_\nu$), set of candidate AoDs $\{\boldsymbol{\phi}_s\}_{s=0}^{N_\phi - 1}$
**Output:** $\hat{\boldsymbol{\phi}}$ and $\hat{v}_{\mathrm{r}}$

1: $\boldsymbol{F} \leftarrow N_\nu \times L/2$ DFT matrix
2: **for** $s \in \{0, \ldots, N_\phi - 1\}$ **do**
3: **for** $k \in \{0, \ldots, L/2\}$ **do**
4: $[\boldsymbol{z}_s]_k = \boldsymbol{a}(\theta)^\top \mathrm{diag}(\boldsymbol{b}_k) \boldsymbol{a}(\boldsymbol{\phi}_s)$
5: $\boldsymbol{w}_s = \boldsymbol{z}_s / \|\boldsymbol{z}_s\|$
6: $\boldsymbol{g}_s = \boldsymbol{w}_s^* \odot \boldsymbol{z}_\phi$
7: $\boldsymbol{h}_s = \boldsymbol{F} \boldsymbol{g}_s$
8: $[i_{\mathrm{m}}, s_{\mathrm{m}}] \leftarrow \max_{i,s} |[\boldsymbol{h}_s]_i|$
9: $\hat{\boldsymbol{\phi}} \leftarrow \boldsymbol{\phi}_{s_{\mathrm{m}}}$
10: **if** $i_{\mathrm{m}} > N_\nu/2$ **then**
11: $i_{\mathrm{m}} \leftarrow i_{\mathrm{m}} - N_\nu + 1$
12: $\hat{v}_{\mathrm{r}} \leftarrow i_{\mathrm{m}} \lambda / (2 T_{\mathrm{sym}} N_\nu)$
13: **return** $\hat{\boldsymbol{\phi}}$ and $\hat{v}_{\mathrm{r}}$

**Algorithm 5** *Direct_Par_Est($\boldsymbol{Y}$)*

**Inputs:** Signal ($\boldsymbol{Y} \in \mathbb{C}^{N\times L}$)
**Output:** Estimation of parameters for the direct path: gain $\hat{g}_{\mathrm{b}}$, radial velocity $\hat{v}_{\mathrm{b}}$, and delay $\hat{\tau}_{\mathrm{b}}$

1: $\boldsymbol{w}_{\mathrm{b}} \leftarrow [1, 1]^\top$
2: $\boldsymbol{Z}_{\mathrm{b}} \leftarrow$ *match*$(\boldsymbol{Y}, \boldsymbol{w}_{\mathrm{b}})$
3: $\hat{v}_b \leftarrow$ *Coarse_Velocity_Est*$(\boldsymbol{Z}_{\mathrm{b}})$
4: $\hat{v}_b \leftarrow$ *Fine_Velocity_Est*$(\boldsymbol{Z}_{\mathrm{b}}, \hat{v}_b)$
5: $\boldsymbol{T}_{\mathrm{b}} \leftarrow \left(\boldsymbol{F}\boldsymbol{E}(\hat{v}_{\mathrm{b}})^{-1} \boldsymbol{F}^{\mathrm{H}} \boldsymbol{Y}\right) \odot \boldsymbol{C}(\hat{v}_{\mathrm{b}})^*$
6: $\hat{\boldsymbol{Z}}_{\mathrm{b}} \leftarrow$ *match*$(\boldsymbol{T}_{\mathrm{b}}, \boldsymbol{w}_{\mathrm{b}})$
7: $\boldsymbol{z}_\tau \leftarrow \sum_t [\hat{\boldsymbol{Z}}_{\mathrm{b}}]_{:,t}$
8: $\hat{\tau}_{\mathrm{b}} \leftarrow$ *Coarse_delay_Est*$(\boldsymbol{z}_\tau)$
9: $\hat{\tau}_{\mathrm{b}} \leftarrow$ *Fine_delay_Est*$(\boldsymbol{z}_\tau, \hat{\tau}_{\mathrm{b}})$
10: $\hat{g}_{\mathrm{b}} \leftarrow [\boldsymbol{D}(\hat{\tau}_{\mathrm{b}})]_{:,1}^{\mathrm{H}} \boldsymbol{z}_\tau / (NL)$
11: **return** $\hat{g}_{\mathrm{b}}, \hat{v}_{\mathrm{b}}$, and $\hat{\tau}_{\mathrm{b}}$

### D. Estimation of channel parameters for the direct path

Algorithm 5 presents the estimation of channel parameters for the direct path based on some of the previous algorithms. The input is the received OFDM signal $\boldsymbol{Y}$. First $\boldsymbol{w}_{\mathrm{b}}$ is used to extract the direct signal. Next, we estimate the value of $v_{\mathrm{b}}$, which requires solving a non-convex optimization. We solve this problem by first obtaining a coarse estimation in Line 3. In Line 4, we use the *refinement* step described in Sec. V-A using $\hat{v}_{\mathrm{b}}$ as the initial value. Then, the effects of UE mobility on the direct signal are compensated for and once again the direct signal is extracted via the vector $\boldsymbol{w}_{\mathrm{b}}$ in Line 6. By compensating for the effects of UE mobility, we reduce the residual interference and energy loss in the *matching* process (see Section IV). One can see that the matrix $\hat{\boldsymbol{Z}}_{\mathrm{b}}$ in Line 6 is an estimate of $\boldsymbol{Z}_{\mathrm{b}}$ in (36). The matrix $\hat{\boldsymbol{Z}}_{\mathrm{b}}$ is then summed across time to establish $\boldsymbol{z}_\tau \in \mathbb{C}^N$. One can see that $\boldsymbol{z}_\tau$ has the structure $L g_{\mathrm{b}} [\boldsymbol{D}(\tau_{\mathrm{b}})]_{:,1}$. Therefore, we use $\boldsymbol{z}_\tau$ to estimate $\tau_{\mathrm{b}}$ and then we use $\hat{\tau}_{\mathrm{b}}$ and $\boldsymbol{z}_\tau$ to estimate $g_{\mathrm{b}}$ in Line 10.

**Algorithm 6** *Reflected_Par_Est*($\hat{\boldsymbol{Y}}_{\mathrm{r}}, \{\boldsymbol{b}_0, \dots \boldsymbol{b}_{L/2-1}\}$)

**Inputs:** Signal ($\hat{\boldsymbol{Y}}_{\mathrm{r}} \in \mathbb{C}^{N\times L}$), beams $\{\boldsymbol{b}_k\}$
**Parameters:** Number of iterations $N_{\mathrm{iter}}$
**Output:** Estimation of parameters for the reflected path: AoD $\hat{\phi}$, radial velocity $\hat{v}_{\mathrm{r}}$, delay $\hat{\tau}_{\mathrm{r}}$

1: $\boldsymbol{w}_{\mathrm{r}} \leftarrow [1,-1]^{\top}$
2: $\hat{\boldsymbol{Z}}_{\mathrm{r}} \leftarrow$ *match*$(\hat{\boldsymbol{Y}}_{\mathrm{r}}, \boldsymbol{w}_{\mathrm{r}})$
3: $\hat{\tau}_{\mathrm{r}} \leftarrow$ *Coarse_delay_Est*$(\hat{\boldsymbol{Z}}_{\mathrm{r}})$
4: $\boldsymbol{T}_{\mathrm{r}} \leftarrow \hat{\boldsymbol{Z}}_{\mathrm{r}} \odot [D(\hat{\tau}_{\mathrm{r}})^*]_{:,0:L/2-1}$
5: $\boldsymbol{z}_{\phi} \leftarrow \sum_n [\boldsymbol{T}_{\mathrm{r}}]^{\top}_{n,:}$
6: $[\hat{\phi}, \hat{v}_{\mathrm{r}}] \leftarrow$ *Coarse_Velocity_Angle_Est*$(\boldsymbol{z}_{\phi}, \{\boldsymbol{b}_k\})$
7: **for** $i \in \{0, \dots, N_{\mathrm{iter}}\}$ **do**
8: $\quad \hat{\boldsymbol{Y}}_{\mathrm{rs}} \leftarrow \left(\boldsymbol{F}\boldsymbol{E}(\hat{v}_{\mathrm{r}})^{-1}\boldsymbol{F}^{\mathrm{H}}\hat{\boldsymbol{Y}}_{\mathrm{r}}\right) \odot \boldsymbol{C}(\hat{v}_{\mathrm{r}})^*$
9: $\quad \hat{\boldsymbol{Z}}_{\mathrm{rs}} \leftarrow$ *match*$(\hat{\boldsymbol{Y}}_{\mathrm{rs}}, \boldsymbol{w}_{\mathrm{r}})$
10: $\quad \hat{\tau}_{\mathrm{r}} \leftarrow$ *Fine_delay_Est*$(\hat{\boldsymbol{Z}}_{\mathrm{rs}}, \hat{\tau}_{\mathrm{r}})$
11: $\quad \boldsymbol{T}_{\mathrm{rs}} \leftarrow \hat{\boldsymbol{Z}}_{\mathrm{rs}} \odot [D(\hat{\tau}_{\mathrm{r}})^*]_{:,0:L/2-1}$
12: $\quad \boldsymbol{z}_{\phi} \leftarrow \sum_n [\boldsymbol{T}_{\mathrm{rs}}]_{n,:}$
13: $\quad [\Delta\hat{v}_{\mathrm{r}}, \hat{\boldsymbol{\phi}}] \leftarrow$ *Fine_Velocity_Angle_Est*$(\boldsymbol{z}_{\phi}, 0, \hat{\boldsymbol{\phi}}, \{\boldsymbol{b}_k\})$
14: $\quad \hat{v}_{\mathrm{r}} = \hat{v}_{\mathrm{r}} + \Delta\hat{v}_{\mathrm{r}}$
15: **return** $\hat{\phi}, \hat{v}_{\mathrm{r}}$, and $\hat{\tau}_{\mathrm{r}}$

### *E. Estimation of channel parameters for the reflected path*

In this section, we use some of the previous algorithms to estimate the channel parameters for the reflected path. The process is described in Algorithm 6. The input matrix $\hat{\boldsymbol{Y}}_{\mathrm{r}}$ is an estimate of $\boldsymbol{Y}_{\mathrm{r}}$ in (17). First, we match the signal with the vector $\boldsymbol{w}_{\mathrm{r}}$ to reduce the temporal dimension of the input signal from $L$ to $L/2$, without loss of information and also to remove any interference from the direct path (or possible scatterers). Then, we estimate $\tau_{\mathrm{r}}$ in Line 3 and then compensate for its effects in Line 4. Next, we neglect the spatial-WB effects and assume that the effects of $v_{\mathrm{r}}$, and $\boldsymbol{\phi}_{\mathrm{r}}$ are constant across the subcarriers. Therefore, to estimate these parameters we perform a summation across all subcarriers to obtain $\boldsymbol{z}_{\boldsymbol{\phi}} \in \mathbb{C}^{L/2}$. Assuming the spatial-NB model (see Section III-B), one can see that $\boldsymbol{z}_{\boldsymbol{\phi}}$ has the structure at the RHS of (49). Therefore, we use $\boldsymbol{z}_{\boldsymbol{\phi}}$ to estimate $v_{\mathrm{r}}$ and $\boldsymbol{\phi}_{\mathrm{r}}$ jointly in Line 6. Next, we compensate for the effects of UE mobility via $\hat{v}_{\mathrm{r}}$ in Line 8. This reduces the interpath interference and the energy loss due to the UE mobility. The steps from Line 9 to Line 13 refine the estimations obtained in Lines 2–6 (using the corresponding *refinement* steps in Sec.V-A–V-C)[4]. However, since the effects of velocity have been already compensated for in Line 8, we estimate the residual velocity $\Delta\hat{v}$ (with zero as the initial estimate) in Line 13, which is then added to the coarse estimation. This process is repeated $N_{\mathrm{iter}}$ times to obtain an accurate estimation, where $N_{\mathrm{iter}}$ is a design parameter. Alternatively, one can also stop the iterations after the difference between the estimated velocities becomes less than a certain threshold.

[4]The extra inputs serve as initial values for the quasi-Newton algorithm. Specifically *Fine_Velocity_Angle_Est*$(\boldsymbol{z}_{\phi}, 0, \hat{\boldsymbol{\phi}}, \{\boldsymbol{b}_k\})$ uses the initial values 0 and $\hat{\boldsymbol{\phi}}$ for searching along the velocity and AoD dimensions, respectively.

### *F. Estimation of UE position*

Algorithm 7 explains how to estimate the position of the UE via geometrical channel parameters. First, we calculate the direction of the UE based on $\hat{\boldsymbol{\phi}}$ in Line 2. Next, based on (3) and (4), we can estimate the distance between the UE and the RIS by minimizing the function $f(d)$, defined in Line 3.

**Algorithm 7** *Position_Est*$(\hat{\tau}_{\mathrm{b}}, \hat{\tau}_{\mathrm{r}}, \hat{\boldsymbol{\phi}})$

**Inputs:** Estimation of the ToAs ($\hat{\tau}_{\mathrm{b}}$,$\hat{\tau}_{\mathrm{r}}$) and AoD ($\hat{\boldsymbol{\phi}}$)
**Output:** $\hat{\boldsymbol{p}}$

1: $\Delta r \leftarrow c|\hat{\tau}_{\mathrm{r}} - \hat{\tau}_{\mathrm{b}}|$
2: $\boldsymbol{k} \leftarrow \begin{bmatrix} \sin([\hat{\boldsymbol{\phi}}]_{\mathrm{el}})\cos([\hat{\boldsymbol{\phi}}]_{\mathrm{az}}) \\ \sin([\hat{\boldsymbol{\phi}}]_{\mathrm{el}})\sin([\hat{\boldsymbol{\phi}}]_{\mathrm{az}}) \\ \cos([\hat{\boldsymbol{\phi}}]_{\mathrm{el}}) \end{bmatrix}$
3: $f(d) \leftarrow (d + \|\boldsymbol{p}_{\mathrm{b}} - \boldsymbol{p}_{\mathrm{r}}\| - \|\boldsymbol{p}_{\mathrm{b}} - \boldsymbol{p}_{\mathrm{r}} - d\boldsymbol{k}\| - \Delta r)^2$
4: $d_{\mathrm{m}} \leftarrow \min_d f(d)$
5: $\hat{\boldsymbol{p}} \leftarrow d_{\mathrm{m}}\boldsymbol{k}$
6: **return** $\hat{\boldsymbol{p}}$

### *G. Overall process*

The overall estimation process is described in Algorithm 8. First, the direct channel parameters are estimated in Line 1. Next, we obtain an estimation of the direct signal and remove it from the received signal to obtain an estimate of the reflected one, which is used to obtain estimates of the reflected channel parameters. Next, we use the estimate of the geometrical channel parameters to find the UE position. Finally, in Line 5, we use (3) to estimate the UE clock bias.

*Complexity:* Algorithm 8 has a low complexity compared to a search over all the possible values of the channel parameters to maximize the likelihood function, which requires a 6-dimensional search (the optimal values of the gains can be calculated in closed-form). Note that our estimator performs at most a 3-dimensional search at each step. Specifically, Algorithms 2 and 3 (and their corresponding refinement step) each apply only one line search each to find an estimation of the radial velocity and delay, respectively. Algorithm 4 searches over the possible radial velocities and also the AoDs (elevations and azimuths), consequently, the search is performed over a 3D space, while its corresponding refinement step applies a 1D and a 2D search. Furthermore, we significantly reduced the complexity of our 3D search by using FFT for searching over velocities and 2D FFT method to search over possible AoDs (see Appendix C). Therefore, the proposed algorithm requires much less computational power compared to the maximum-likelihood estimator.

## VI. Simulation results

In this section, we assess the accuracy of our estimation method and compare it to the CRB for a system example with default parameters listed in Table I. The algorithm parameters are set to $N_{\tau} = 4096$ (the IDFT dimension for delay estimation in Algorithm 3) and $N_{\mathrm{v}} = N_{\nu} = 256$ (the

**Algorithm 8** *Estimator*$(\boldsymbol{Y}, \{\boldsymbol{b}_0, \dots \boldsymbol{b}_{L/2-1}\})$

**Inputs:** Received signal ($\boldsymbol{Y} \in \mathbb{C}^{N\times L}$), beams $\{\boldsymbol{b}_k\}$
**Output:** Estimation of UE position ($\hat{\boldsymbol{p}}$), UE clock bias $\hat{\Delta}_t$, and radial velocities $\hat{v}_\mathrm{b}, \hat{v}_\mathrm{r}$

1: $[\hat{g}_\mathrm{b}, \hat{v}_\mathrm{b}, \hat{\tau}_\mathrm{b}] \leftarrow$*Direct_Par_Est*$(\boldsymbol{Y})$
2: $\hat{\boldsymbol{Y}}_\mathrm{r} \leftarrow \boldsymbol{Y} - \hat{g}_\mathrm{b}\boldsymbol{F}\boldsymbol{E}(\hat{v}_\mathrm{b})\boldsymbol{F}^\mathrm{H}(\boldsymbol{D}(\hat{\tau}_\mathrm{b}) \odot \boldsymbol{C}(\hat{v}_\mathrm{b}))$
3: $[\hat{\phi}, \hat{v}_\mathrm{r}, \hat{\tau}_\mathrm{r}] \leftarrow$*Reflected_Par_Est*$(\hat{\boldsymbol{Y}}_\mathrm{r}, \{\boldsymbol{b}_0, \dots \boldsymbol{b}_{L/2-1}\})$
4: $\hat{\boldsymbol{p}} \leftarrow$ *Position_Est*$(\hat{\tau}_\mathrm{b}, \hat{\tau}_\mathrm{r}, \hat{\boldsymbol{\phi}})$
5: $\hat{\Delta}_t \leftarrow \hat{\tau}_\mathrm{b} - \|\hat{\boldsymbol{p}} - \boldsymbol{p}_\mathrm{b}\|/c$
6: **return** $\hat{\boldsymbol{p}}$, $\hat{\Delta}_t$, $\hat{v}_\mathrm{b}$, and $\hat{v}_\mathrm{r}$

TABLE I: Parameters used in the simulation.

| Parameter | Symbol | Value |
|---|---|---|
| RIS dimensions | $M_1 \times M_2$ | $64 \times 64$ |
| Wavelength | $\lambda$ | 1 cm |
| RIS element distance | $d$ | 0.5 cm |
| Light speed | $c$ | $3 \times 10^8$ m/s |
| Number of subcarriers | $N$ | 3 000 |
| Subcarrier bandwidth | $\Delta_f$ | 120 kHz |
| Symbol duration | $T$ | 8.33 us |
| CP duration | $T_\mathrm{cp}$ | 0.58 us |
| Number of transmissions | $L$ | 256 |
| Transmission Power | $N\Delta F E_\mathrm{s}$ | 20 dBm |
| Noise PSD | $N_0$ | $-174$ dBm/Hz |
| UE's Noise figure | $n_f$ | 8 dB |
| Noise variance | $\sigma^2 = n_f N_0$ | $-166$ dBm/Hz |
| BS position | $\boldsymbol{p}_\mathrm{b}$ | $[5, 5, 0]$ |
| RIS position | $\boldsymbol{p}_\mathrm{r}$ | $[0, 0, 0]$ |
| Uncertainty radius | $\sigma$ | 1m |

DFT dimension for velocity estimation in Algorithms 3 and 4, respectively). The number of candidate AoDs in Algorithm 4 is set to $N_\phi = 256$ when using the directional profiles or $N_\phi = 256^2$ for the random profiles, and the selection of candidate AoDs are done according to Appendix C. Also, the number of iterations in Algorithm 6 is set to[5] $N_\mathrm{itr} = 3$. The RIS is located at the origin such that the local coordinates of RIS matches the global coordinate system ($\boldsymbol{R}$ is the identity matrix). Following the widely used assumption of quasi-static channel over a coherence interval[6] [16], [56]–[60] (consisting of $L$ OFDM symbols), the channel gains are assigned random phases (fixed during $L$ symbols) and the amplitudes are calculated as [61, Eq. (21)–(23)]

$$|g_\mathrm{b}| = \frac{\lambda\sqrt{E_\mathrm{s}}}{4\pi\|\boldsymbol{p}_\mathrm{b} - \boldsymbol{p}\|} \tag{54}$$

$$|g_\mathrm{r}| = \frac{\lambda^2 \cos^q(\alpha_\theta)\cos^q(\alpha_\phi)\sqrt{E_\mathrm{s}}}{16\pi\|\boldsymbol{p}_\mathrm{b} - \boldsymbol{p}_\mathrm{r}\|\|\boldsymbol{p}_\mathrm{r} - \boldsymbol{p}\|} \tag{55}$$

with $q = 0.285$ (see [61]), where $E_\mathrm{s}$ indicates the pilot energy, and $\alpha_\phi$ and $\alpha_\theta$ are defined below (28). Before presenting the results, in Section VI-A, we present some preliminary information about the calculation of the CRB based on Fisher information matrix (FIM) analysis, which will be used as a benchmark in this section. Then, we study the spatial-WB effects in Section VI-B for different RIS sizes and signal bandwidths. Next in Section VI-C the mobility effects are considered and the influence of the uncertainty radius as well as scatterers are shown in Section VI-D.

[5]Based on our simulation results (not provided in this paper), for the considered parameters, the position error saturates after two iterations.

[6]The UE mobility affects the time-varying phase of the received signal through Doppler-induced phase progressions in fast-time and slow-time domains, modeled by (23) and (22), respectively.

### A. FIM analysis

FIM analysis can be used to develop theoretical lower bounds on the estimation error of any unbiased estimator. We do so by calculating the FIM first for the channel parameters and then for the positional parameters. We define the set of channel parameters as

$$\boldsymbol{\zeta}_\mathrm{ch} = [\tau_\mathrm{b}, \tau_\mathrm{r}, [\boldsymbol{\phi}]_\mathrm{az}, [\boldsymbol{\phi}]_\mathrm{el}, v_\mathrm{b}, v_\mathrm{r}, \Re(g_\mathrm{b}), \Im(g_\mathrm{b}), \Re(g_\mathrm{r}), \Im(g_\mathrm{r})]^\top. \tag{56}$$

The FIM can be calculated as follows [62]

$$\boldsymbol{F}_\mathrm{ch} = \frac{2}{\sigma^2}\sum_{t=0}^{L-1}\sum_{n=0}^{N-1} \mathrm{Re}\left\{\frac{\partial[\boldsymbol{M}]_{n,t}}{\partial\boldsymbol{\zeta}_\mathrm{ch}}\left(\frac{\partial[\boldsymbol{M}]_{n,t}}{\partial\boldsymbol{\zeta}_\mathrm{ch}}\right)^\mathrm{H}\right\}, \tag{57}$$

where $\boldsymbol{M}$ is the noiseless part of the received signal. In this paper, we use the dynamic spatial-wideband model in (16)–(17) to compute (57) unless stated otherwise. Next, we calculate the FIM for positional parameters, that is

$$\boldsymbol{\zeta}_\mathrm{po} = [\boldsymbol{p}^\top, \Delta t, v_\mathrm{b}, v_\mathrm{r}, \Re(g_\mathrm{b}), \Im(g_\mathrm{b}), \Re(g_\mathrm{r}), \Im(g_\mathrm{r})]^\top. \tag{58}$$

We do so, by calculating $\boldsymbol{F}_\mathrm{po} = \boldsymbol{J}^\top\boldsymbol{F}_\mathrm{ch}\boldsymbol{J}$, where the Jacobian matrix $\boldsymbol{J} \in \mathbb{R}^{10\times 10}$ is defined as

$$\boldsymbol{J}_{\ell,s} = \frac{\partial[\boldsymbol{\zeta}_\mathrm{ch}]_\ell}{\partial[\boldsymbol{\zeta}_\mathrm{po}]_s}. \tag{59}$$

By obtaining $\boldsymbol{F}_\mathrm{ch}$ the estimation error of the $m$th channel parameter is lower bounded as

$$\mathrm{E}(|[\boldsymbol{\zeta}_\mathrm{ch}]_m - \widehat{[\boldsymbol{\zeta}_\mathrm{ch}]}_m|^2) \geq [\boldsymbol{F}_\mathrm{ch}^{-1}]_{m,m}, \tag{60}$$

where $\widehat{[\boldsymbol{\zeta}_\mathrm{ch}]}_m$ indicates the estimate of the parameter $[\boldsymbol{\zeta}_\mathrm{ch}]_m$. Similarly the estimation of the positional parameters can be bounded using $\boldsymbol{F}_\mathrm{po}$. Furthermore, we use the position error bound (PEB) as a lower bound on the position estimation error, that is

$$\sqrt{\left[\mathrm{E}(\|\boldsymbol{p} - \hat{\boldsymbol{p}}\|^2)\right]} \geq \sqrt{\mathrm{trace}([\boldsymbol{F}_\mathrm{po}^{-1}]_{1:3,1:3})}. \tag{61}$$

The derivatives required for calculating $\boldsymbol{F}_\mathrm{ch}$ and $\boldsymbol{J}$ can be calculated based on the relations described in Section II.

We note that for the directional codebook, the prior information of the UE position affects the FIM only through the beamforming, and we do not take into account the effects of the fusion of the estimated position and the prior information. Since the proposed estimator also does not perform information fusion, the presented PEB correctly lower-bounds the position error of our estimator.

### B. Wideband effects

In this section, we study the accuracy of our estimator in presence of spatial-WB effects using numerical results. To do so, we calculate the PEB and evaluate the UE position estimation error considering the random and directional RIS profiles described in Section IV-C. We place the UE at $[-r/\sqrt{2}, r/\sqrt{2}, -10]$ for $r \in [2, 100]$ (in meters). Figure 3

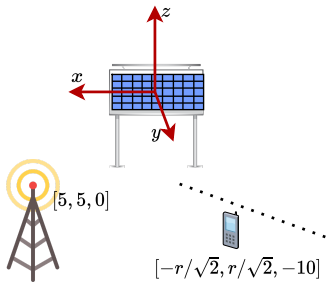


Fig. 3: Placement of the RIS, BS, and UE in the 3D space.

demonstrates the placement of BS, RIS, and UE in the 3D space. Furthermore, in Fig. 4 we consider the data transmission through the spatial-WB channel in (16)–(17) and also the spatial-NB one in (24)–(25). For each point, we average the results over 20 sets of RIS phase profiles, for each of which we consider 20 noise realizations.

Fig. 4 (a) presents the results for $M = 64^2$ and $N = 3000$. It can be seen that with the NB channel, the estimator attains the PEB at every point. With the WB channel, the estimator has a noticeably larger error compared to the PEB for low values of $r$. The reason is that for low values of $r$ the angle $\alpha$ in (28) becomes large and the assumption (28) does not hold. Therefore, the mismatch between the WB and the NB channels becomes considerable, and the accuracy of the estimator (which is designed based on the NB channel) deteriorates. Furthermore, one can observe that the PEBs for the WB and NB channel models are almost equal, which shows that the performance degradation can be compensated by adopting a better (and more complex) estimator. Future research can aim to prove mathematically (via FIM analysis) that the changes of PEB due to user mobility and spatial WB effects are indeed negligible.

In Fig. 4 (a), it can be seen that the estimation error due to spatial-WB effects has a more pronounced effect for directional beamforming than the random one, which is mainly due to higher SNRs in the directional case which makes the influence of the distortion caused by the spatial-WB effects more pronounced. Fig. 4 (b) and Fig. 4 (c), present the same results for a system with half of the RIS size and half of the bandwidth of the system considered in Fig. 4 (a). Apart from a natural degradation in localization accuracy, it can be seen that the WB effects diminish. This can be justified by (28). Also, we note that for large values of $r$ and random beamforming the estimation error in Fig. 4 (b) cannot follow the PEB due to low values of SNR.

In Fig. 5, we demonstrate the position error for the UE location at $[-5/\sqrt{2}, -5/\sqrt{2}, -10]$ for a large range of the received SNR of the direct path. It can be seen that for SNRs lower than $0$ dBm, the estimator fails to estimate the UE location for random RIS profiles. Also, it can be seen that at high SNRs the estimation error saturates for both directional and random phase profiles due to the spatial WB effects. Based on our simulation results (not included in this paper), similar behavior can also be observed for the estimation error of the AOD.

To study the WB effects more closely in Fig. 6, we present the PEB and the estimation errors at $r = 5$ for a large range of signal bandwidth ($B = N\Delta_f$). As can be seen, the PEBs decrease with $B$, which shows that a better localization performance can be attained with higher bandwidths. However, our estimator, which is designed based on the NB model, does not show such behavior. Specifically with the directional beamforming, after $B = 140$ MHz the distortion caused by the WB effects causes a higher positioning error.

### C. Mobility effects

Fig. 7 presents the cumulative distribution functions (CDFs) of the estimation error and the CRB for $100$ different realizations of random and directional RIS phase profiles. For each RIS phase profile we generated $1000$ noise realizations to accurately calculate the estimation error. We consider two UE velocities: One where UE is static and one where the UE velocity vector is set to $\boldsymbol{v} = [-30, 30, 0]\,\mathrm{m/s}$. We consider the estimation of the UE position in Fig. 7 (a), UE clock bias in Fig. 7 (b), and UE radial velocity vector $v_\mathrm{r}$ in Fig. 7 (c). The velocity vector is estimated based on the radial velocities and the relations (1) and (2) and by assuming that the estimator has the prior knowledge that $[\boldsymbol{v}]_3 = 0$.

It can be seen from Fig. 7 that in addition to the UE position, the UE velocity vector and also the UE clock bias can be estimated. Therefore, the UE can be synchronized to the BS. There is a small reduction in the accuracy of velocity estimation for the high-mobility user compared to the static one. This is due to the error in position estimation which causes error in the estimation of $\boldsymbol{v}$ from the estimated radial velocities, $\hat{v}_\mathrm{b}$ and $\hat{v}_\mathrm{r}$. Apart from this, it is apparent that the UE velocity does not affect the estimation accuracy, both in terms of analytical bounds and also estimation error. This can be explained based on the fact that the UE radial velocities can be estimated with the accuracy of up to $0.1\,\mathrm{m/s}$ and then their effects can be removed from the received signal.

### D. Uncertainty radius and scatterers

Fig. 8 demonstrates the CDF of the position error for $100$ realizations of the directional RIS beams for different values of $\sigma$. It can be seen that the optimal performance among the considered values of $\sigma$ is obtained by $\sigma = 0.5\,\mathrm{m}$. For very small values of $\sigma$ (like $\sigma = 0.1\,\mathrm{m}$), all the transmitted beams become almost similar to each other and therefore accurate AoD estimation cannot be performed due to lack of beam diversity. Furthermore, with larger values of $\sigma$ there is a probability that none of the transmitted beams hits the UE, which results in low SNR and high estimation error. This is the reason why the CDF of the estimation error becomes saturated around $0.95$ for $\sigma = 3\mathrm{m}$. Furthermore, we examine the performance of our estimator in presence of $10$ scatterers, whose radio cross sections are equal to $0.1\ \mathrm{m}^2$ and are distributed randomly on a disc placed on the $z = -11$ plane, centered at $[0, 0, -11]$ with $5$ meters radius. The channel gains for scatterers are calculated based on the radar range equation (see e.g., [61, Eq. (23)]). It can be seen that although the presence of the scatterers can degrade the localization accuracy, it is still possible to perform cm-level positioning.

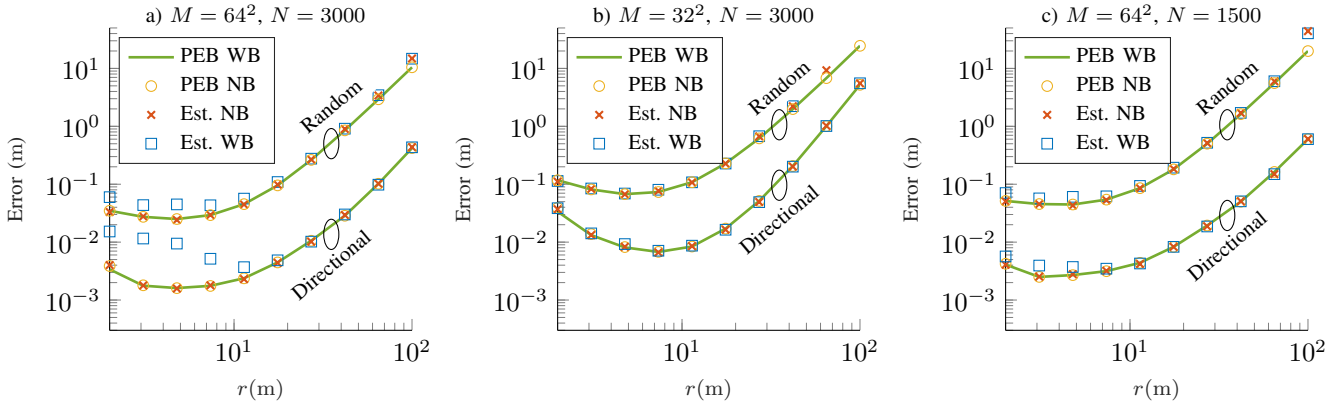


Fig. 4: Estimation error and the CRB bounds for UE position along the path $[-r/\sqrt{2}, r/\sqrt{2}, -10]$, where $r$ varies between 2m to 100m considering NB and WB models, and directional and random RIS phase profiles. Results are presented for different combinations of the number of RIS elements ($M$) and subcarriers ($N$): a) $M = 64^2$, $N = 3000$, b) $M = 32^2$, $N = 3000$, c) $M = 64^2$, $N = 1500$.

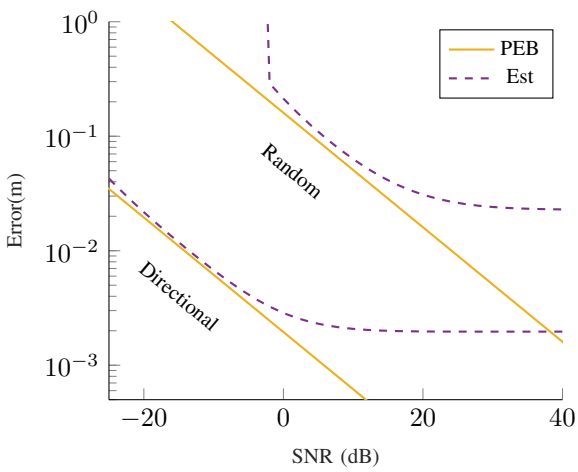


Fig. 5: Position error for the UE position $[-5/\sqrt{2}, -5/\sqrt{2}, -10]$ for directional and random RIS phase profiles vs the received SNR (of the direct path).

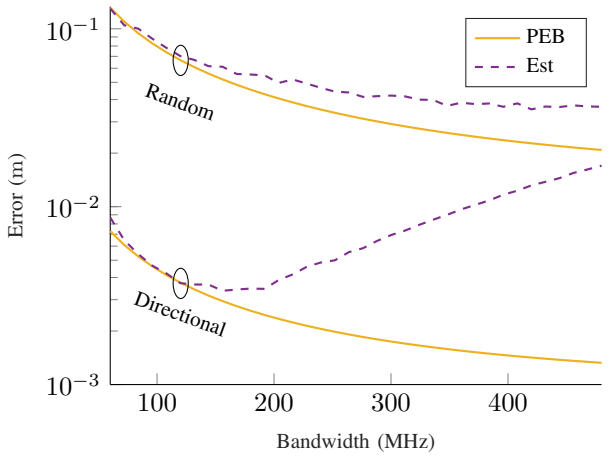


Fig. 6: Estimation error and CRB bounds for the UE position at $[-5/\sqrt{2}, 5/\sqrt{2}, -10]$ as a function of signal bandwidth ($B$). Directional and random phase profiles were considered.

## VII. Conclusion

We analyzed the influence of UE mobility and spatial-WB effects on the accuracy of an RIS-enabled SISO system by deriving CRB and also devising an estimator. Based on our numerical results, it was shown that the UE mobility does not have any notable effects on the estimation accuracy of the UE state. This was shown in Fig. 7, where both the bounds and the estimation errors are virtually equal for a static UE and a UE with a very high speed. Our proposed estimator dealt with the UE mobility by successively estimating the radial velocities and compensating for their effects. Our results suggest that the studies that assume static users can be potentially extended to account for the UE mobility without any significant performance degradation. With regard to spatial-WB effects it was shown that these effects do not change the analytical bounds and therefore the performance of the optimal estimator. However, for a low-complexity estimator that ignores the spatial-WB effects (such as the one presented in this work), they can degrade the localization accuracy, especially for large signal bandwidth and RIS sizes. Specifically, it was shown in Fig.6 that for some typical system values increasing the number of subcarriers can decrease the estimation accuracy indicating the existence of an optimal signal bandwidth. This result shows the importance of devising a low-complexity estimator that can cope with the spatial-WB effects in dynamic systems, which is an interesting topic for future research.

## Appendix A
## Spatial-Wideband Model under UE Mobility

In this appendix, we derive the received signal coming through the reflected path ($\boldsymbol{Y}_{\mathrm{r}}$) by taking into account spatial-WB effects [41], [46]–[48] and UE mobility [32], [33], [35], [63]. The received signal from the direct path ($\boldsymbol{Y}_{\mathrm{b}}$) in (16) can be derived in the same fashion. We use the same notation as in Section II. In addition, for the derivations, we adopt an approach similar to those in [41], [47], [64], where we compute the total path delay between the BS and the UE, including the BS-to-RIS delay, the (adjustable) delay at the RIS and the RIS-to-UE delay, along with the Doppler effects due to UE mobility.

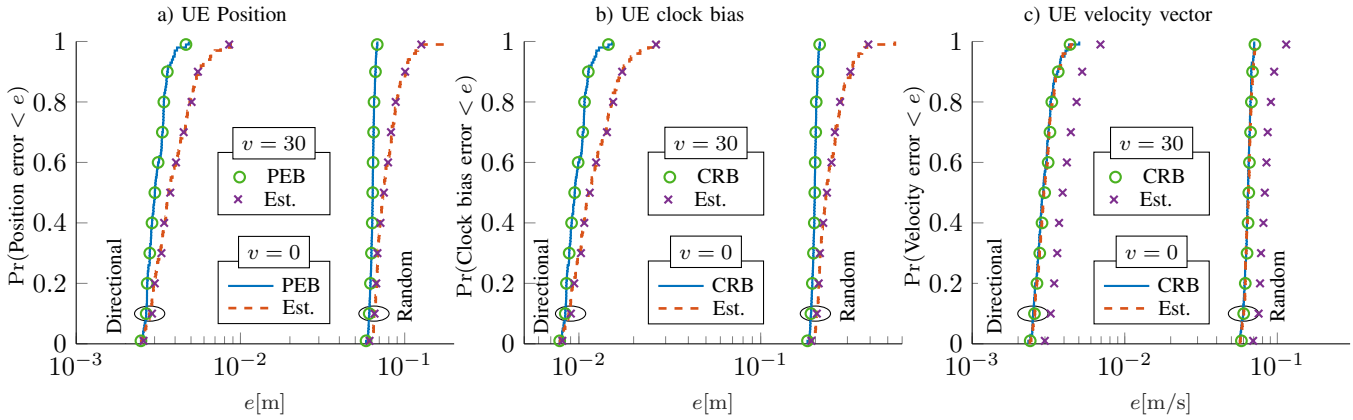


Fig. 7: CDF of estimation error and CRB bounds for 100 realizations of directional and random RIS phase profiles for a) UE position, b) UE clock bias, and c) UE velocity $\boldsymbol{v}$. The UE has the position $[-10, 10, -10]$ and velocity $[-v, v, 0]$, where $v \in \{0, 30\}$m/s.

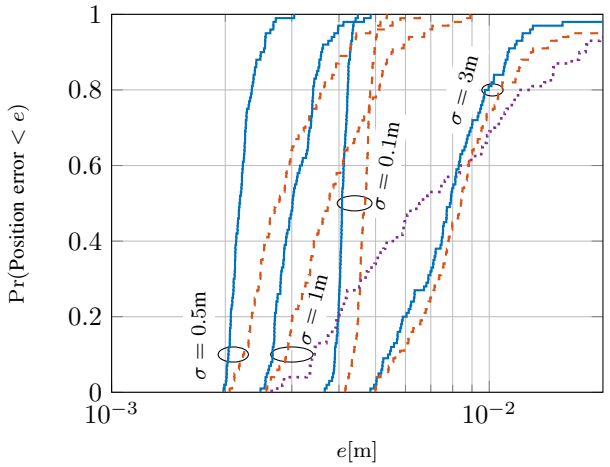


Fig. 8: CDF of estimation error (dashed lines) and CRB bounds (solid lines) for 100 realizations of directional RIS phase profiles constructed based on different uncertainty radii ($\sigma$). The estimation error for $\sigma = 1$m in presence of 10 scatterers is also shown (the dotted line). The UE has the position $[-10, 10, -10]$.

### A. Transmit signal model

The transmitted OFDM baseband signal can be expressed as

$$s(t) = \sum_{\ell=0}^{L-1} s_\ell(t), \tag{62}$$

where

$$s_\ell(t) = \frac{1}{\sqrt{N}} \sum_{n=0}^{N-1} x_{n,\ell}\, e^{\jmath 2\pi n \Delta_f t} \text{rect}\left(\frac{t - \ell T_{\text{sym}}}{T_{\text{sym}}}\right) \tag{63}$$

denotes the OFDM signal for the $\ell$th symbol, $x_{n,\ell}$ is the complex pilot symbol on the $n$th subcarrier for the $\ell$th symbol, and rect $(t)$ is a rectangular function that takes the value 1 for $t \in [0, 1)$ and 0 otherwise. Then, the upconverted transmit signal can be written as

$$s_{\text{u}}(t) = \Re\left\{s(t) e^{\jmath 2\pi f_c t}\right\}. \tag{64}$$

### B. Receive signal model

Based on the transmit signal model in (64), the passband received signal at the UE due to the reflected path through the RIS is given by [47]

$$y_{\text{ur}}(t) = \Re\left\{\widetilde{g}_{\text{r}} \sum_{m=0}^{M-1} s(t - [\boldsymbol{\tau}(t)]_m) e^{\jmath 2\pi f_c (t - [\boldsymbol{\tau}(t)]_m)}\right\}, \tag{65}$$

where $\widetilde{g}_{\text{r}}$ is the complex path gain and the vector $\boldsymbol{\tau}(t) \in \mathbb{R}^M$ contains the delays between the BS and the UE through the different elements of the RIS. It can be computed as

$$\boldsymbol{\tau}(t) = \boldsymbol{\tau}_{\text{br}} + \boldsymbol{\tau}_{\text{r}}(t) + \boldsymbol{\tau}_{\text{ru}}(t) + \Delta_t, \tag{66}$$

where the vector $\boldsymbol{\tau}_{\text{br}}$ contains the delays between the BS and the elements of the RIS

$$[\boldsymbol{\tau}_{\text{br}}]_m = \frac{\|\boldsymbol{p}_{\text{b}} - \boldsymbol{p}_{\text{r},m}\|}{c} \tag{67}$$

with $\boldsymbol{p}_{\text{r},m}$ denoting the location of the $m$th RIS element, $[\boldsymbol{\tau}_{\text{r}}(t)]_m$ denotes the delay incurred by the $m$th element of the RIS at time $t$ [64], $[\boldsymbol{\tau}_{\text{ru}}(t)]_m = [\boldsymbol{\tau}_{\text{ru}}]_m - \nu_{\text{r}} t$ represents the time-varying delay [33] from the $m$th element to the UE with $\nu_{\text{r}} = v_{\text{r}}/c$ and $v_{\text{r}}$ denoting the radial velocity along the RIS-UE direction in (2) and

$$[\boldsymbol{\tau}_{\text{ru}}]_m = \frac{\|\boldsymbol{p}_{\text{r},m} - \boldsymbol{p}\|}{c} \tag{68}$$

is the initial delay (at $t = 0$). The complex baseband received signal after downconversion of (65) can be written as [47]

$$y_{\text{r}}(t) = \widetilde{g}_{\text{r}} \sum_{m=0}^{M-1} s(t - [\boldsymbol{\tau}(t)]_m) e^{-\jmath 2\pi f_c [\boldsymbol{\tau}(t)]_m}. \tag{69}$$

Plugging (62) and (63) into (69), we have

$$y_{\text{r}}(t) = \widetilde{g}_{\text{r}} \sum_{m=0}^{M-1} \sum_{\ell=0}^{L-1} \frac{1}{\sqrt{N}} \sum_{n=0}^{N-1} x_{n,\ell}\, e^{\jmath 2\pi n \Delta_f (t - [\boldsymbol{\tau}(t)]_m)} \times e^{-\jmath 2\pi f_c [\boldsymbol{\tau}(t)]_m} \text{rect}\left(\frac{t - [\boldsymbol{\tau}(t)]_m - \ell T_{\text{sym}}}{T_{\text{sym}}}\right). \tag{70}$$

For the $\ell$th symbol, we sample $y_{\text{r}}(t)$ in (70) at $t = \ell T_{\text{sym}} + T_{\text{cp}} + \tau_{\min} + k T_{\text{o}}/N$ for $k = 0, \ldots, N-1$ (i.e., we remove the

CP and sample the interval corresponding to the elementary OFDM signal), where

$$\tau_{\min} = \min_{m} [\boldsymbol{\tau}(0)]_m \tag{71}$$

is the arrival time of the reflected path with respect to the receiver's clock (which can be detected[7], e.g., via downlink synchronization signals [65]). Substituting (66) into (70), the discrete-time signal for the $k$th sample of the $\ell$th symbol at the receiver becomes

$$\begin{aligned}[\widetilde{\boldsymbol{Y}}_{\mathrm{r}}]_{k,\ell} = \widetilde{g}_{\mathrm{r}} \sum_{m=0}^{M-1} \frac{1}{\sqrt{N}} \sum_{n=0}^{N-1} \Big[ & x_{n,\ell}\, e^{\jmath 2\pi n \Delta_f (\ell T_{\mathrm{sym}} + T_{\mathrm{cp}} + \tau_{\min} + kT_{\mathrm{o}}/N)} \\ & \times e^{-\jmath 2\pi n \Delta_f ([\boldsymbol{\tau}_{\mathrm{br}}]_m + [\boldsymbol{\tau}_{\mathrm{r},\ell}]_m + [\boldsymbol{\tau}_{\mathrm{ru}}]_m + \Delta_t)} \\ & \times e^{\jmath 2\pi n \Delta_f \nu_{\mathrm{r}} (\ell T_{\mathrm{sym}} + T_{\mathrm{cp}} + \tau_{\min} + kT_{\mathrm{o}}/N)} \\ & \times e^{-\jmath 2\pi f_c ([\boldsymbol{\tau}_{\mathrm{br}}]_m + [\boldsymbol{\tau}_{\mathrm{r},\ell}]_m + [\boldsymbol{\tau}_{\mathrm{ru}}]_m + \Delta_t)} \\ & \times e^{\jmath 2\pi f_c \nu_{\mathrm{r}} (\ell T_{\mathrm{sym}} + T_{\mathrm{cp}} + \tau_{\min} + kT_{\mathrm{o}}/N)} \Big] \end{aligned} \tag{72}$$

under the assumption that $[\boldsymbol{\tau}(0)]_m - \tau_{\min} \leq T_{\mathrm{cp}}$, which holds in practice since the UE is in the far-field of RIS and the RIS delays $\boldsymbol{\tau}_{\mathrm{r}}$ are very small compared to propagation delays $[\boldsymbol{\tau}_{\mathrm{br}}]_m$ and $[\boldsymbol{\tau}_{\mathrm{ru}}]_m$ [64]. In (72), it is assumed that the RIS profile can change across OFDM symbols and $[\boldsymbol{\tau}_{\mathrm{r},\ell}]_m = [\boldsymbol{\tau}_{\mathrm{r}}(\ell T_{\mathrm{sym}} + T_{\mathrm{cp}})]_m$ represents the delay of the $m$th element corresponding to the RIS configuration applied for the $\ell$th symbol.

Since the receiver's clock reference can be set to an arbitrary known epoch, we can set $\tau_{\min} = 0$. The received signal in (72) can be written as

$$\begin{aligned}[\widetilde{\boldsymbol{Y}}_{\mathrm{r}}]_{k,\ell} = & \frac{\widetilde{g}_{\mathrm{r}}}{\sqrt{N}} e^{\jmath 2\pi f_c \nu_{\mathrm{r}} (T_{\mathrm{cp}} + kT_{\mathrm{o}}/N)} \sum_{n=0}^{N-1} \widetilde{x}_{n,\ell} e^{\jmath 2\pi n k/N} \\ & \times e^{\jmath 2\pi (f_c + n\Delta_f) \nu_{\mathrm{r}} \ell T_{\mathrm{sym}}} e^{\jmath 2\pi n \Delta_f \nu_{\mathrm{r}} (T_{\mathrm{cp}} + kT_{\mathrm{o}}/N)} \\ & \times \sum_{m=0}^{M-1} e^{-\jmath 2\pi (f_c + n\Delta_f)([\boldsymbol{\tau}_{\mathrm{br}}]_m + [\boldsymbol{\tau}_{\mathrm{r},\ell}]_m + [\boldsymbol{\tau}_{\mathrm{ru}}]_m + \Delta_t)}, \end{aligned} \tag{73}$$

where

$$\widetilde{x}_{n,\ell} = x_{n,\ell} e^{\jmath 2\pi n \Delta_f (\ell T_{\mathrm{sym}} + T_{\mathrm{cp}})}. \tag{74}$$

We define the phase shift induced by the delay $[\boldsymbol{\tau}_{\mathrm{r},\ell}]_m$ at the center frequency as $\psi_{\ell,m} = 2\pi f_c [\boldsymbol{\tau}_{\mathrm{r},\ell}]_m$, which we assume to be less than $2\pi$ (note that the choice of the RIS configuration $[\boldsymbol{\tau}_{\mathrm{r},\ell}]_m$ is under the designer's control [64] and $[\boldsymbol{\tau}_{\mathrm{r},\ell}]_m \in [0, 1/f_c)$ will cover all possible phase shifts).

To make (73) more compact, we will now rely on the following approximations/simplifications:

1) *frequency-narrowband approximation:*

$$\frac{f_c + n\Delta_f}{f_c} \psi_{\ell,m} \approx \psi_{\ell,m}, \tag{75}$$

which holds as long as $B/f_c \ll 1$ (which is satisfied in our simulations according to Table I with $B = 360\,\mathrm{MHz}$ and $f_c = 30\,\mathrm{GHz}$).

2) *far-field approximation*[8]*:*

$$2\pi (f_c + n\Delta_f)(\boldsymbol{\tau}_{\mathrm{br}} - \tau_{\mathrm{br}}) \approx -\boldsymbol{k}^{\top}(\boldsymbol{\theta}) \boldsymbol{Q} \tag{76}$$

$$2\pi (f_c + n\Delta_f)(\boldsymbol{\tau}_{\mathrm{ru}} - \tau_{\mathrm{ru}}) \approx -\boldsymbol{k}^{\top}(\boldsymbol{\phi}) \boldsymbol{Q}, \tag{77}$$

where $\tau_{\mathrm{br}} = \|\boldsymbol{p}_{\mathrm{b}} - \boldsymbol{p}_{\mathrm{r}}\|/c$, $\tau_{\mathrm{ru}} = \|\boldsymbol{p}_{\mathrm{r}} - \boldsymbol{p}\|/c$, and $\boldsymbol{k}$ and $\boldsymbol{Q}$ are defined in (15) and (14), respectively.

3) *negligible phase term under practical velocity values*[9]*:*

$$e^{\jmath 2\pi n \Delta_f \nu_{\mathrm{r}} (T_{\mathrm{cp}} + kT_{\mathrm{o}}/N)} \approx 1. \tag{78}$$

In addition, we define $[\boldsymbol{\gamma}_\ell]_m = e^{-\jmath \psi_{\ell,m}}$ to indicate the RIS phase profile, and a constant phase reference $\psi_r \triangleq 2\pi f_c \tau_{\mathrm{r}}$. Using (75)–(77), the last summation in (73) can be written as

$$\begin{aligned} & \sum_{m=0}^{M-1} e^{-\jmath 2\pi (f_c + n\Delta_f)([\boldsymbol{\tau}_{\mathrm{br}}]_m + [\boldsymbol{\tau}_{\mathrm{r},\ell}]_m + [\boldsymbol{\tau}_{\mathrm{ru}}]_m + \Delta_t)} \qquad (79) \\ & = \sum_{m=0}^{M-1} e^{-\jmath 2\pi (f_c + n\Delta_f)([\boldsymbol{\tau}_{\mathrm{br}}]_m - \tau_{\mathrm{br}})} e^{-\jmath 2\pi (f_c + n\Delta_f)([\boldsymbol{\tau}_{\mathrm{ru}}]_m - \tau_{\mathrm{ru}})} \\ & \quad \times e^{-\jmath 2\pi (f_c + n\Delta_f)(\tau_{\mathrm{br}} + \tau_{\mathrm{ru}} + \Delta_t)} e^{-\jmath 2\pi (f_c + n\Delta_f)[\boldsymbol{\tau}_{\mathrm{r},\ell}]_m} \\ & \approx e^{-\jmath 2\pi n \Delta_f \tau_{\mathrm{r}}} e^{-\jmath \psi_r} \sum_{m=0}^{M-1} e^{\jmath \boldsymbol{k}(\boldsymbol{\theta})^{\top} [\boldsymbol{Q}]_{:,m}} e^{\jmath \boldsymbol{k}(\boldsymbol{\phi})^{\top} [\boldsymbol{Q}]_{:,m}} [\boldsymbol{\gamma}_\ell]_m \\ & = e^{-\jmath 2\pi n \Delta_f \tau_{\mathrm{r}}} e^{-\jmath \psi_r} \sum_{m=0}^{M-1} [\boldsymbol{a}(\boldsymbol{\theta})]_m [\boldsymbol{\gamma}_\ell]_m [\boldsymbol{a}(\boldsymbol{\phi})]_m \\ & = e^{-\jmath 2\pi n \Delta_f \tau_{\mathrm{r}}} e^{-\jmath \psi_r} [\boldsymbol{A}(\boldsymbol{\phi})]_{n,\ell}\ , \qquad (80) \end{aligned}$$

where the matrix $\boldsymbol{A}(\boldsymbol{\phi})$ is defined in (11) and $\tau_{\mathrm{r}}$ in (4).

By substituting (80) and (78) into (73), we obtain

$$\begin{aligned}[\widetilde{\boldsymbol{Y}}_{\mathrm{r}}]_{k,\ell} = & \frac{g_{\mathrm{r}}}{\sqrt{N}} e^{\jmath 2\pi v_{\mathrm{r}} kT_{\mathrm{o}}/(\lambda N)} \sum_{n=0}^{N-1} \widetilde{x}_{n,\ell} e^{\jmath 2\pi n k/N} \\ & \times e^{\jmath 2\pi v_{\mathrm{r}} \ell T_{\mathrm{sym}}/\lambda_n} e^{-\jmath 2\pi n \Delta_f \tau_{\mathrm{r}}} [\boldsymbol{A}(\boldsymbol{\phi})]_{n,\ell}. \end{aligned} \tag{81}$$

Here, we used $(f_c + n\Delta_f)\nu_{\mathrm{r}} = v_{\mathrm{r}}(f_c + n\Delta_f)/c = v_{\mathrm{r}}/\lambda_n$, where $\lambda_n$ is defined in (21). Also, we have

$$g_{\mathrm{r}} = \widetilde{g}_{\mathrm{r}} e^{\jmath 2\pi f_c \nu_{\mathrm{r}} T_{\mathrm{cp}}} e^{-\jmath \psi_{\mathrm{r}}}. \tag{82}$$

Assuming $\widetilde{x}_{n,\ell} = 1$ for all[10] $n$ and $\ell$, the summation in (81) can be written via the DFT matrix $\boldsymbol{F}$ in (18) as

$$\widetilde{\boldsymbol{Y}}_{\mathrm{r}} = g_{\mathrm{r}} \boldsymbol{E}(v_{\mathrm{r}}) \boldsymbol{F}^{\mathrm{H}} \left( \boldsymbol{D}(\tau_{\mathrm{r}}) \odot \boldsymbol{A}(\boldsymbol{\phi}) \odot \boldsymbol{C}_{\mathrm{w}}(v_{\mathrm{r}}) \right), \tag{83}$$

where $\boldsymbol{D}(\tau)$, $\boldsymbol{C}_{\mathrm{w}}(v)$ and $\boldsymbol{E}(v)$ are defined, respectively, in (10), (22) and (23). Finally, we define

$$\boldsymbol{Y}_{\mathrm{r}} = \boldsymbol{F} \widetilde{\boldsymbol{Y}}_{\mathrm{r}} \tag{84}$$

to obtain (17).

[7]Since the variation of the delays $\boldsymbol{\tau}(t)$ across the RIS elements could be much smaller than the delay resolution, the UE can possibly identify a single correlation peak contributed by all the RIS elements, in which case $\tau_{\min}$ is set as the location of that peak.

[8]The far-field approximation in (76) (and, similarly, the one in (77)) can be readily derived by observing that, in the far-field regime, the difference between the BS-to-RIS center distance and the BS-to-$m$-th RIS element distance can be written as a function of $\boldsymbol{\theta}$, the AoA from the BS to RIS, and $[\boldsymbol{Q}]_{:,m}$, the position of the $m$-th RIS element relative to the RIS center.

[9]The phase of the left hand side (LHS) of (78) can be upper bounded with $2\pi B T_{\mathrm{sym}} v_{\mathrm{r}}/c$, which for the values in Table I and $v_{\mathrm{r}} = 30\,\mathrm{m/s}$ is about $2 \cdot 10^{-3}$.

[10]According to (74), the pilot symbols $x_{n,\ell}$ can be chosen such that $\widetilde{x}_{n,\ell} = 1$ for the sake of simplicity of analysis. The signal model can be straightforwardly extended to the case of arbitrary pilot symbols. In addition, the effects of transmit power can be modeled by adjusting the noise variance in (7).

## APPENDIX B
## CONDITIONS OF VALIDITY FOR SPATIAL-NARROWBAND APPROXIMATION IN (24)–(25)

In this part, we derive the conditions under which the spatial-narrowband approximation in (24)–(25) is valid. To this end, we explore when $\boldsymbol{C}_{\mathrm{w}}(v)$ and $\boldsymbol{A}_{\mathrm{w}}(\boldsymbol{\phi})$ in the spatial-wideband model (16)–(17) can be approximated as $\boldsymbol{C}(v)$ and $\boldsymbol{A}(\boldsymbol{\phi})$ in the spatial-narrowband model (24)–(25), respectively.

### A. Condition of Validity for Approximation of (22)

For the transition from $[\boldsymbol{C}_{\mathrm{w}}(v)]_{n,\ell}$ in (22) to $[\boldsymbol{C}(v)]_{n,\ell}$ in (26) to be valid, the following approximation must hold $\forall \ell, n$:

$$e^{\jmath 2\pi \ell T_{\mathrm{sym}} v/\lambda_n} \approx e^{\jmath 2\pi \ell T_{\mathrm{sym}} v/\lambda} \ , \tag{85}$$

which requires

$$e^{\jmath 2\pi \ell T_{\mathrm{sym}} v(f_c+n\Delta_f)/c} \approx e^{\jmath 2\pi \ell T_{\mathrm{sym}} v f_c/c} \tag{86a}$$

$$e^{\jmath 2\pi \ell T_{\mathrm{sym}} v n\Delta_f/c} \approx 1 \tag{86b}$$

$$LT_{\mathrm{sym}} Bv \ll c \tag{86c}$$

$$LNv \ll c \tag{86d}$$

$$LN\max\{v_{\mathrm{r}}, v_{\mathrm{b}}\} \ll c \ , \tag{86e}$$

where (86c) is obtained by plugging the worst-case conditions $\ell = L-1$ and $n = N-1$ (in terms of approximation quality) into (86b) and recalling that $B = N\Delta_f$, (86d) results from $BT_{\mathrm{sym}} \approx BT = B/\Delta_f = N$ (assuming $T_{\mathrm{cp}}/T$ is small), and (86e) follows by considering the maximum of direct and reflected path velocities.

### B. Condition of Validity for Approximation of (19)

Similarly, for the transition from $[\boldsymbol{A}_{\mathrm{w}}(\boldsymbol{\phi})]_{n,\ell}$ in (19) to $[\boldsymbol{A}(\boldsymbol{\phi})]_{n,\ell}$ in (11) to be valid, we need

$$e^{\jmath \boldsymbol{k}_n(\boldsymbol{\psi})^\top [\boldsymbol{Q}]_{:,m}} \approx e^{\jmath \boldsymbol{k}(\boldsymbol{\psi})^\top [\boldsymbol{Q}]_{:,m}} \tag{87}$$

for any $n$ and the angles $\boldsymbol{\psi} \in \{\boldsymbol{\theta}, \boldsymbol{\phi}\}$, which represent, respectively, the AoA and AoD for the RIS in (19). From (15) and the definition of $\boldsymbol{q}_{r,s}$ in Sec. II-A, this requires

$$e^{\jmath \max(M_1,M_2) d\sin(\alpha) 2\pi/\lambda_n} \approx e^{\jmath \max(M_1,M_2) d\sin(\alpha) 2\pi/\lambda} \tag{88a}$$

$$e^{\jmath \max(M_1,M_2) d\sin(\alpha) 2\pi (f_c+n\Delta_f)/c} \approx e^{\jmath \max(M_1,M_2) d\sin(\alpha) 2\pi f_c/c} \tag{88b}$$

$$e^{\jmath \max(M_1,M_2) d\sin(\alpha) 2\pi n\Delta_f/c} \approx 1 \tag{88c}$$

$$\max(M_1,M_2) d\sin(\alpha) B \ll c \ , \tag{88d}$$

where $\alpha$ denotes the angle between the RIS normal ($[0,1,0]^\top$) and the vector $\boldsymbol{k}(\boldsymbol{\psi})$[11], and (88d) follows by considering the worst-case scenario (in terms of approximation quality) $n = N-1$.

## APPENDIX C
## CHOOSING THE CANDIDATE AODS

In this section, we explain how we select the AoDs $\boldsymbol{\phi}$. For the case with existing prior location information $\boldsymbol{\xi}$ (see Section IV-C2), we choose $N_\phi$ points within the sphere centered at $\boldsymbol{\xi}$ with radius $\sigma$ (similarly as in Section IV-C2). Then the set $\{\boldsymbol{\phi}_s\}_{s=0}^{N_\phi-1}$ is calculated as the angles from the RIS towards these points. Furthermore, with directional beams in (43) the calculation of $\boldsymbol{z}_s$ in Line 4 of Algorithm 4 can be performed in closed-form (the RHS of Line 4 reduces to a geometric sum), which reduces the complexity of Algorithm 4.

In the absence of any prior information about the user, the values of $\boldsymbol{z}_s$ can be calculated offline since the beams can be set prior to the localization procedure. Furthermore, to reduce the complexity of calculating $\boldsymbol{z}_s$, we use 2D inverse fast Fourier transform (IFFT), which is explained as follows. We re-write the vector $\boldsymbol{a}(\boldsymbol{\psi})$ in (13) as

$$\boldsymbol{a}(\boldsymbol{\psi}) = \boldsymbol{a}_1(\boldsymbol{\psi}) \otimes \boldsymbol{a}_2(\boldsymbol{\psi}), \tag{89}$$

where

$$\boldsymbol{a}_1(\boldsymbol{\psi}) = e^{\jmath\beta_1}[1, e^{\jmath[\boldsymbol{k}(\boldsymbol{\psi})]_1 d}, \ldots, e^{\jmath[\boldsymbol{k}(\boldsymbol{\psi})]_1 (M_1-1)d}] \tag{90}$$

$$\boldsymbol{a}_2(\boldsymbol{\psi}) = e^{\jmath\beta_2}[1, e^{\jmath[\boldsymbol{k}(\boldsymbol{\psi})]_3 d}, \ldots, e^{\jmath[\boldsymbol{k}(\boldsymbol{\psi})]_3 (M_2-1)d}], \tag{91}$$

where $\beta_1 = [\boldsymbol{k}(\boldsymbol{\psi})]_1 (M_1-1)d/2$ and $\beta_2 = [\boldsymbol{k}(\boldsymbol{\psi})]_3 (M_2-1)d/2$. Next, from Line 4 we have that

$$[\boldsymbol{z}_s]_k = \boldsymbol{a}(\theta)^\top \mathrm{diag}(\boldsymbol{b}_k) \boldsymbol{a}(\boldsymbol{\phi}_s) \tag{92}$$

$$= \boldsymbol{a}(\boldsymbol{\phi}_s)^\top (\boldsymbol{a}(\theta) \odot \boldsymbol{b}_k) \tag{93}$$

$$= e^{\jmath(\beta_1+\beta_2)} \boldsymbol{a}_1(\boldsymbol{\phi}_s)^\top \boldsymbol{C}_k \boldsymbol{a}_2(\boldsymbol{\phi}_s), \tag{94}$$

where

$$\boldsymbol{C}_k = \left(\boldsymbol{a}_1(\theta)\boldsymbol{a}_2(\theta)^\top\right) \odot \boldsymbol{B}_k \tag{95}$$

and (94) follows from (89) and the properties of the Kronecker product (see [66, Eq. (520)]). Motivated by (89), we set $\boldsymbol{z}_s$ to be the $s$th row of matrix $\boldsymbol{Z}_{\mathrm{f}} = [\boldsymbol{z}_{\mathrm{f},0}, \ldots, \boldsymbol{z}_{\mathrm{f},L/2-1}]$, where

$$\boldsymbol{z}_{\mathrm{f},k} = \mathrm{vec}\left(\boldsymbol{F}_{\phi,1}^\top \boldsymbol{C}_k \boldsymbol{F}_{\phi,2}\right). \tag{96}$$

Here, $\boldsymbol{F}_{\phi,1} \in \mathbb{C}^{M_1 \times N_{\phi,1}}$ and $\boldsymbol{F}_{\phi,2} \in \mathbb{C}^{M_2 \times N_{\phi,1}}$ are IDFT matrices, where $N_{\phi,1}$ and $N_{\phi,2}$ are design parameters. Furthermore, the RHS of (96) can be calculated using 2D IFFT. The set $\{\boldsymbol{\phi_s}\}$ can be calculated as $\{\boldsymbol{\phi}_{0,0}, \boldsymbol{\phi}_{1,0}, \ldots, \boldsymbol{\phi}_{N_{\phi,1}-1, N_{\phi,2}-1}\}$, where

$$[\boldsymbol{\phi}_{n_1,n_2}]_{\mathrm{az}} = \mathrm{atan2}\left(k_2(n_1,n_2), k_1(n_1,n_2)\right) \tag{97}$$

$$[\boldsymbol{\phi}_{n_1,n_2}]_{\mathrm{el}} = \mathrm{acos}\left(k_3(n_1,n_2)\right). \tag{98}$$

Here,

$$k_1(n_1,n_2) = f_{\mathrm{r}}\left(\frac{\lambda n_1}{dN_{\phi,1}}\right) \tag{99}$$

$$k_3(n_1,n_2) = f_{\mathrm{r}}\left(\frac{\lambda n_2}{dN_{\phi,2}}\right) \tag{100}$$

$$k_2(n_1,n_2) = \sqrt{1-k_1^2-k_3^2}, \tag{101}$$

where the function $f_{\mathrm{r}} = x - 2\lfloor x/2 \rfloor$ compensates for the wrap-around effects. Furthermore, for the values of $n_1$ and $n_2$ if $k_2(n_1,n_2)$ becomes imaginary $\boldsymbol{\phi}_{n_1,n_2}$ is undefined and the estimator can remove these values from the sets $\{\boldsymbol{z}_s\}$ and $\{\boldsymbol{\phi}_s\}$.

[11]Note that $[\boldsymbol{Q}]_{:,m}$ is orthogonal to the RIS normal; therefore, only the component of $\boldsymbol{k}(\boldsymbol{\psi})$ that is orthogonal to the RIS normal contributes to the value of $\boldsymbol{k}(\boldsymbol{\psi})^\top [\boldsymbol{Q}]_{:,m}$. This component has the norm $\sin(\alpha)$.

## REFERENCES


[1] K. Keykhosravi, M. F. Keskin, G. Seco-Granados, and H. Wymeersch, "SISO RIS-enabled joint 3D downlink localization and synchronization," in *Proc. IEEE ICC*, Montreal, Canada, Jun. 2021.

[2] A. Bourdoux, A. N. Barreto, B. van Liempd, C. de Lima, D. Dardari, D. Belot, E.-S. Lohan, G. Seco-Granados, H. Sarieddeen, H. Wymeersch *et al.*, "6G white paper on localization and sensing," *arXiv preprint arXiv:2006.01779*, 2020.

[3] "Feasibility of positioning enhancements for E-UTRA, release 13, V13.0.0," 3GPP TR 36.855, Jan. 2015.

[4] A. Shahmansoori, G. E. Garcia, G. Destino, G. Seco-Granados, and H. Wymeersch, "Position and orientation estimation through millimeter-wave MIMO in 5G systems," *IEEE Trans. Wireless Commun.*, vol. 17, no. 3, pp. 1822–1835, Mar. 2018.

[5] C. Pan, H. Ren, K. Wang, J. F. Kolb, M. Elkashlan, M. Chen, M. Di Renzo, Y. Hao, J. Wang, A. L. Swindlehurst, X. You, and L. Hanzo, "Reconfigurable intelligent surfaces for 6G systems: Principles, applications, and research directions," *IEEE Commun. Mag.*, vol. 59, no. 6, pp. 14–20, 2021.

[6] M. Di Renzo, A. Zappone, M. Debbah, M.-S. Alouini, C. Yuen, J. de Rosny, and S. Tretyakov, "Smart radio environments empowered by reconfigurable intelligent surfaces: How it works, state of research, and the road ahead," *IEEE J. Select. Areas Commun.*, vol. 38, no. 11, pp. 2450–2525, Nov. 2020.

[7] E. Basar, M. Di Renzo, J. De Rosny, M. Debbah, M. Alouini, and R. Zhang, "Wireless communications through reconfigurable intelligent surfaces," *IEEE Access*, vol. 7, pp. 116 753–116 773, Sep. 2019.

[8] M. Najafi, V. Jamali, R. Schober, and H. V. Poor, "Physics-based modeling and scalable optimization of large intelligent reflecting surfaces," *IEEE Transactions on Communications*, vol. 69, no. 4, pp. 2673–2691, 2021.

[9] X. Yuan, Y.-J. A. Zhang, Y. Shi, W. Yan, and H. Liu, "Reconfigurable-intelligent-surface empowered wireless communications: Challenges and opportunities," *IEEE Wireless Communications*, vol. 28, no. 2, pp. 136–143, 2021.

[10] C. Huang, A. Zappone, G. C. Alexandropoulos, M. Debbah, and C. Yuen, "Reconfigurable intelligent surfaces for energy efficiency in wireless communication," *IEEE Transactions on Wireless Communications*, vol. 18, no. 8, pp. 4157–4170, 2019.

[11] W. Tang, M. Z. Chen, X. Chen, J. Y. Dai, Y. Han, M. Di Renzo, Y. Zeng, S. Jin, Q. Cheng, and T. J. Cui, "Wireless communications with reconfigurable intelligent surface: Path loss modeling and experimental measurement," *IEEE Transactions on Wireless Communications*, vol. 20, no. 1, pp. 421–439, 2021.

[12] A. L. Swindlehurst, G. Zhou, R. Liu, C. Pan, and M. Li, "Channel estimation with reconfigurable intelligent surfaces–a general framework," *arXiv preprint:2110.00553*, 2021.

[13] G. T. de Araújo, A. L. F. de Almeida, and R. Boyer, "Channel estimation for intelligent reflecting surface assisted MIMO systems: A tensor modeling approach," *IEEE J. Select. Topics Signal Process.*, vol. 15, no. 3, pp. 789–802, 2021.

[14] Z. Wang, L. Liu, and S. Cui, "Channel estimation for intelligent reflecting surface assisted multiuser communications: Framework, algorithms, and analysis," *IEEE Transactions on Wireless Communications*, vol. 19, no. 10, pp. 6607–6620, 2020.

[15] Z.-Q. He and X. Yuan, "Cascaded channel estimation for large intelligent metasurface assisted massive MIMO," *IEEE Wireless Communications Letters*, vol. 9, no. 2, pp. 210–214, 2020.

[16] Y. Yang, B. Zheng, S. Zhang, and R. Zhang, "Intelligent reflecting surface meets OFDM: Protocol design and rate maximization," *IEEE Transactions on Communications*, vol. 68, no. 7, pp. 4522–4535, 2020.

[17] Q. Wu and R. Zhang, "Intelligent reflecting surface enhanced wireless network via joint active and passive beamforming," *IEEE Transactions on Wireless Communications*, vol. 18, no. 11, pp. 5394–5409, 2019.

[18] A. Elzanaty, A. Guerra, F. Guidi, and M.-S. Alouini, "Reconfigurable intelligent surfaces for localization: Position and orientation error bounds," *IEEE Transactions on Signal Processing*, vol. 69, pp. 5386–5402, 2021.

[19] D. Dardari, N. Decarli, A. Guerra, and F. Guidi, "Localization in NLOS conditions using large reconfigurable intelligent surfaces," in *Proc. IEEE SPAWC*, Sep. 2021.

[20] M. Rahal, B. Denis, K. Keykhosravi, B. Uguen, and H. Wymeersch, "RIS-enabled localization continuity under near-field conditions," in *Proc. IEEE SPAWC*, Jun. 2021.

[21] K. Keykhosravi, M. F. Keskin, S. Dwivedi, G. Seco-Granados, and H. Wymeersch, "Semi-passive 3D positioning of multiple RIS-enabled users," *IEEE Transactions on Vehicular Technology*, vol. 70, no. 10, pp. 11 073–11 077, 2021.

[22] H. Zhang, H. Zhang, B. Di, K. Bian, Z. Han, and L. Song, "Towards ubiquitous positioning by leveraging reconfigurable intelligent surface," *IEEE Communications Letters*, vol. 25, no. 1, pp. 284–288, 2021.

[23] H. Zhang, H. Zhang, B. Di, K. Bian, Z. Han, C. Xu, D. Zhang, and L. Song, "RSS fingerprinting based multi-user outdoor localization using reconfigurable intelligent surfaces," in *Proc. IEEE ISMICT*, Apr. 2021.

[24] S. Hu, F. Rusek, and O. Edfors, "Beyond massive MIMO: The potential of positioning with large intelligent surfaces," *IEEE Trans. Signal Process.*, vol. 66, no. 7, pp. 1761–1774, Apr. 2018.

[25] Y. Liu *et al.*, "Reconfigurable intelligent surface aided wireless localization," in *Proc. IEEE ICC*, Montreal, Canada, Jun. 2021.

[26] J. V. Alegría and F. Rusek, "Cramér-rao lower bounds for positioning with large intelligent surfaces using quantized amplitude and phase," in *Proc. Asilomar CSSC*, Pacific Grove, USA, Nov. 2019, pp. 10–14.

[27] H. Zhang, J. Hu, H. Zhang, B. Di, K. Bian, Z. Han, and L. Song, "Metaradar: Indoor localization by reconfigurable metamaterials," *IEEE Transactions on Mobile Computing*, 2020.

[28] Z. Abu-Shaban, K. Keykhosravi, M. F. Keskin, G. C. Alexandropoulos, G. Seco-Granados, and H. Wymeersch, "Near-field localization with a reconfigurable intelligent surface acting as lens," in *IEEE Int. Conf. Commun.*, 2021, pp. 1–6.

[29] O. Rinchi, A. Elzanaty, and M.-S. Alouini, "Compressive near-field localization for multipath RIS-aided environments," *IEEE Commun. Lett.*, pp. 1–1, 2022.

[30] D. Dardari, N. Decarli, A. Guerra, and F. Guidi, "LOS/NLOS near-field localization with a large reconfigurable intelligent surface," *IEEE Trans. Wireless Commun.*, pp. 1–1, 2021.

[31] W. Wang and W. Zhang, "Joint beam training and positioning for intelligent reflecting surfaces assisted millimeter wave communications," *IEEE Trans. Wireless Commun.*, vol. 20, no. 10, pp. 6282–6297, 2021.

[32] B. Matthiesen, E. Björnson, E. De Carvalho, and P. Popovski, "Intelligent reflecting surface operation under predictable receiver mobility: A continuous time propagation model," *IEEE Wireless Commun. Lett.*, vol. 10, no. 2, pp. 216–220, Feb. 2021.

[33] E. Basar, "Reconfigurable intelligent surfaces for doppler effect and multipath fading mitigation," *arXiv preprint arXiv:1912.04080*, 2019.

[34] Z. Huang, B. Zheng, and R. Zhang, "Transforming fading channel from fast to slow: Intelligent refracting surface aided high-mobility communication," *IEEE Transactions on Wireless Communications*, pp. 1–1, 2021.

[35] S. Sun and H. Yan, "Channel estimation for reconfigurable intelligent surface-assisted wireless communications considering Doppler effect," *IEEE Wireless Commun. Lett.*, vol. 10, no. 4, pp. 790–794, Apr. 2021.

[36] C. Xu, J. An, T. Bai, L. Xiang, S. Sugiura, R. G. Maunder, L.-L. Yang, and L. Hanzo, "Reconfigurable intelligent surface assisted multi-carrier wireless systems for doubly selective high-mobility ricean channels," *IEEE Transactions on Vehicular Technology*, pp. 1–1, 2022.

[37] J. Xu and B. Ai, "When mmwave high-speed railway networks meet reconfigurable intelligent surface: A deep reinforcement learning method," *IEEE Wireless Communications Letters*, vol. 11, no. 3, pp. 533–537, 2022.

[38] G. Wu, "Analysis of multi-path fading and the Doppler effect for reconfigurable-intelligent-surface-assisted wireless networks," *Entropy*, vol. 24, no. 2, p. 281, 2022.

[39] K. Wang, C.-T. Lam, and B. K. Ng, "IRS-aided predictable high-mobility vehicular communication with Doppler effect mitigation," in *2021 IEEE 93rd Vehicular Technology Conference (VTC2021-Spring)*, 2021, pp. 1–6.

[40] W. Wu, H. Wang, W. Wang, and R. Song, "Doppler mitigation method aided by reconfigurable intelligent surfaces for high-speed channels," *IEEE Wireless Communications Letters*, vol. 11, no. 3, pp. 627–631, 2022.

[41] B. Wang, F. Gao, S. Jin, H. Lin, and G. Y. Li, "Spatial-and frequency-wideband effects in millimeter-wave massive MIMO systems," *IEEE Trans. Signal Process.*, vol. 66, no. 13, pp. 3393–3406, Jul. 2018.

[42] M. Jian, G. C. Alexandropoulos, E. Basar, C. Huang, R. Liu, Y. Liu, and C. Yuen, "Reconfigurable intelligent surfaces for wireless communications: Overview of hardware designs, channel models, and estimation techniques," *arXiv preprint arXiv:2203.03176*, 2022.

[43] M. Cai, K. Gao, D. Nie, B. Hochwald, J. N. Laneman, H. Huang, and K. Liu, "Effect of wideband beam squint on codebook design in phased-array wireless systems," in *IEEE Global Commun. Conf. (GLOBECOM).*, Washington, DC, USA, Dec. 2016.

[44] K. Dovelos, M. Matthaiou, H. Q. Ngo, and B. Bellalta, "Channel estimation and hybrid combining for wideband terahertz massive MIMO systems," *IEEE J. Select. Areas Commun.*, vol. 39, no. 6, pp. 1604–1620, Jun. 2021.

[45] N. J. Myers and R. W. Heath, "Infocus: A spatial coding technique to mitigate misfocus in near-field LoS beamforming," *IEEE Trans. Wireless Commun.*, pp. 1–1, 2021.

[46] K. Dovelos, S. D. Assimonis, H. Q. Ngo, B. Bellalta, and M. Matthaiou, "Intelligent reflecting surface-aided wideband THz communications: Modeling and analysis," *arXiv preprint: 2110.15768*.

[47] S. Ma, W. Shen, J. An, and L. Hanzo, "Wideband channel estimation for IRS-aided systems in the face of beam squint," *IEEE Trans. Wireless Commun.*, vol. 20, no. 10, pp. 6240–6253, Oct. 2021.

[48] Y. Chen, D. Chen, and T. Jiang, "Beam-squint mitigating in reconfigurable intelligent surface aided wideband mmwave communications," in *IEEE Wireless Commun. Netw. Conf. (WCNC)*, May 2021.

[49] T. Roman, S. Visuri, and V. Koivunen, "Blind frequency synchronization in OFDM via diagonality criterion," *IEEE Transactions on Signal Processing*, vol. 54, no. 8, pp. 3125–3135, 2006.

[50] Y. Ge, W. Zhang, F. Gao, and G. Y. Li, "Frequency synchronization for uplink massive MIMO with adaptive MUI suppression in angle domain," *IEEE Transactions on Signal Processing*, vol. 67, no. 8, pp. 2143–2158, 2019.

[51] Y. Feng, W. Zhang, Y. Ge, and H. Lin, "Frequency synchronization in distributed antenna systems: Pairing-based multi-CFO estimation, theoretical analysis, and optimal pairing scheme," *IEEE Transactions on Communications*, vol. 67, no. 4, pp. 2924–2938, 2018.

[52] G. Hakobyan and B. Yang, "A novel intercarrier-interference free signal processing scheme for OFDM radar," *IEEE Transactions on Vehicular Technology*, vol. 67, no. 6, pp. 5158–5167, 2017.

[53] M. F. Keskin, H. Wymeersch, and V. Koivunen, "MIMO-OFDM joint radar-communications: Is ICI friend or foe?" *IEEE Journal of Selected Topics in Signal Processing*, vol. 15, no. 6, pp. 1393–1408, 2021.

[54] K. Keykhosravi and H. Wymeersch, "Multi-RIS discrete-phase encoding for interpath-interference-free channel estimation," *arXiv preprint arXiv:2106.07065*, Jun. 2021.

[55] H.-H. Chen, J.-F. Yeh, and N. Suehiro, "A multicarrier CDMA architecture based on orthogonal complementary codes for new generations of wideband wireless communications," *IEEE Communications Magazine*, vol. 39, no. 10, pp. 126–135, 2001.

[56] B. Zheng and R. Zhang, "Intelligent reflecting surface-enhanced OFDM: Channel estimation and reflection optimization," *IEEE Wireless Communications Letters*, vol. 9, no. 4, pp. 518–522, 2020.

[57] S. Lin, B. Zheng, G. C. Alexandropoulos, M. Wen, F. Chen, and S. sMumtaz, "Adaptive transmission for reconfigurable intelligent surface-assisted OFDM wireless communications," *IEEE Journal on Selected Areas in Communications*, vol. 38, no. 11, pp. 2653–2665, 2020.

[58] B. Zheng, C. You, and R. Zhang, "Fast channel estimation for IRS-assisted OFDM," *IEEE Wireless Communications Letters*, vol. 10, no. 3, pp. 580–584, 2021.

[59] W. Yang, H. Li, M. Li, Y. Liu, and Q. Liu, "Channel estimation for practical IRS-assisted OFDM systems," in *2021 IEEE Wireless Communications and Networking Conference Workshops (WCNCW)*, 2021, pp. 1–6.

[60] Y. Yang, S. Zhang, and R. Zhang, "IRS-enhanced OFDMA: Joint resource allocation and passive beamforming optimization," *IEEE Wireless Communications Letters*, vol. 9, no. 6, pp. 760–764, 2020.

[61] S. W. Ellingson, "Path loss in reconfigurable intelligent surface-enabled channels," in *IEEE 32nd Annual International Symposium on Personal, Indoor and Mobile Radio Communications (PIMRC)*, 2021, pp. 829–835.

[62] S. M. Kay, *Fundamentals of Statistical Signal Processing: Estimation Theory*. Pearson Education, 2010.

[63] Z. Huang, B. Zheng, and R. Zhang, "Transforming fading channel from fast to slow: IRS-assisted high-mobility communication," in *IEEE Int. Conf. Commun. (ICC)*, Montreal, Canada, Jun. 2021.

[64] E. Björnson, H. Wymeersch, B. Matthiesen, P. Popovski, L. Sanguinetti, and E. de Carvalho, "Reconfigurable intelligent surfaces: A signal processing perspective with wireless applications," *IEEE Signal Processing Magazine*, vol. 39, no. 2, pp. 135–158, 2022.

[65] "3GPP TS 38.211 NR; physical channels and modulation," Tech. Rep., 2020.

[66] K. B. Petersen and M. S. Pedersen, *The Matrix Cookbook*, November 15 2012. [Online]. Available: http://www.math.uwaterloo.ca/~hwolkowi/matrixcookbook.pdf